UC Santa Cruz
UC Santa Cruz Electronic Theses and Dissertations

Title

Characterization of the Effects of N+ Doping Concentration and Dielectric Thickness on the Spatial and Temporal Resolutions of AC-Coupled LGAD Sensors

Permalink
https://escholarship.org/uc/item/7qw1c5n2

Author
Hyslop, Sean

Publication Date
2021

Peer reviewed|Thesis/dissertation

eScholarship.org Powered by the California Digital Library
University of California

UNIVERSITY OF CALIFORNIA
SANTA CRUZ

CHARACTERIZATION OF THE EFFECTS OF N+ DOPING CONCENTRATION AND DIELECTRIC THICKNESS ON THE SPATIAL AND TEMPORAL RESOLUTIONS OF AC-COUPLED LGAD SENSORS

A thesis submitted in partial satisfaction
of the requirements for the degree of

MASTER OF SCIENCE

in

PHYSICS

by

Sean Hyslop

December 2021

The Thesis of Sean Hyslop is
approved:

____
Professor Bruce Schumm

____
Professor Hartmut Sadrozinski

____
Professor Robert Johnson

____
Peter Biehl
Vice Provost and Dean of Graduate Studies

Table of Contents

List of Figures iv

List of Tables v

Abstract vi

Acknowledgements viii

1 Introduction 1

2 Apparatus 7

2.1 Sensors 7

2.2 Readout 8

3 Procedure 10

4 Results and Analysis 12

4.1 Pulse Comparison Between Wafers 12

4.1.1 Pulse Shape n + Comparison 14

4.1.2 Pulse Shape Dielectric Thickness Comparison 18

4.1.3 Summary of Results for Pulse Comparisons 21

4.2 Pulse Delay Comparison 22

4.3 Position Resolution 24

4.3.1 Summary of Results for Position Resolution 35

4.4 Timing Jitter 38

4.4.1 Timing Jitter n + Comparison 41

4.4.2 Timing Jitter Dielectric Thickness Comparison 47

4.4.3 Summary of Results for Timing Jitter 50

5 Summary of Major Results 52

Appendix A. Derivations of Silicon Sensor Signal Properties 55

A.1 Maximum current signal in traditional silicon sensors 55

A.2 Dependence of signal slew rate on sensor gain and thickness 56

A.3 Maximum current signal in silicon sensors with gain 56

References 57

List of Figures

Figure 1.1. Plot of FWHM timing resolution vs. signal to noise ratio from [10] 3

Figure 2.1. Image of sensor geometry studied 7
Figure 2.2. (Left) Fermilab 16 channel amplifier board with all four AC-LGAD wafers mounted. (Right) Microscope picture of mounted sensors on amplifier board. 9

Figure 3.1. Sample scan of maximum pulse heights... 11

Figure 4.1. Red dots represent the locations used to examine average pulse shapes. 14
Figure 4.2. Normalized pulses for wafers 3, 8, and 13 16
Figure 4.3. Undershoots of normalized pulses shown in Figure 4.2.......................... 17
Figure 4.4. Normalized pulses for wafers 3 and 4 19
Figure 4.5. Undershoots of normalized pulses shown in Figure 4.4.......................... 20
Figure 4.6. Overlay of pulses from the locations shown in Figure 4.1 22
Figure 4.7. Normalized P_{max} distributions for wafers 3, 4 ,8, and 13........................ 27
Figure 4.8. Total signal from two adjacent pads for wafers 3, 4, 8, and 13............... 29
Figure 4.9. Total signal-to-noise ratio vs. Position for wafers 3, 4, 8, and 13........... 30
Figure 4.10. P_{max} Fraction vs. Position for wafers 3, 4, 8, and 13 31
Figure 4.11. Position vs. P_{max} Fraction distribution for wafers 3, 4, 8, and 13 32
Figure 4.12. Position Resolution vs. Position for wafers 3, 4, 8, and 13 34
Figure 4.13. Effects of signal noise on comparator threshold crossing time 39
Figure 4.14. Rise time vs. Position for wafers 3, 4, 8, and 13 40
Figure 4.15. Normalized jitter profiles for wafers 3, 8, and 13 42
Figure 4.16. Weighted-average jitter profiles for wafers 3, 8, and 13 46
Figure 4.17. Normalized jitter profiles for wafers 3 and 4 47
Figure 4.18. Weighted-average jitter profiles for wafers 3 and 4 49

List of Tables

Table 1. Fabrication parameters for different wafers of AC-LGADs made by FBK... 8
Table 2. Pulse delay fit results 23
Table 3. Scale factors used to normalize P_{max} distributions 28
Table 4. Fit results for Position vs. P_{max} Fraction distributions................................ 33
Table 5. Comparison of relative differences in position resolution between wafers.. 35

Abstract

Characterization of the Effects of N+ Doping Concentration and Dielectric Thickness on the Spatial and Temporal Resolutions of AC-Coupled LGAD Sensors

by

Sean Hyslop

The next generation of particle detector systems will require sensors that can simultaneously record position and time to great precision. The low gain avalanche detector (LGAD) is a thin n-on-p silicon sensor implementing internal gain which results in a temporal resolution on the order of 10s of picoseconds. However, due to gain layer segmentation, position resolution in LGADs is limited to the millimeter scale. AC-coupled LGADs (AC-LGAD) improve on the position resolution of traditional LGADs through the implementation of a thin dielectric AC-coupling layer between the n^+ implant and readout electrodes, allowing for the use of continuous, planar, n^+ and gain layers. This leads to intrinsic charge sharing between readout electrodes, resulting in a spatial resolution on the order of 10μm. In this thesis, the spatial and temporal resolutions of several AC-LGAD wafers, differing in either n^+ concentration or dielectric thickness, were characterized using the Transient Current Technique with an IR laser set to replicate a MIP. Position resolutions were found to range from 6.9-8.6μm depending on the wafer studied and the position between pads. A straightforward trend relating the wafer fabrication parameters to position resolution was not possible. Timing jitters were found to range from 8.5-13.9ps depending on wafer and position. Overall, it was shown that increasing n^+ concentration (decreasing

sheet resistance) and increasing dielectric thickness (decreasing capacitance) both lead to lower timing jitter.

Acknowledgements

First and foremost, I would like to express my deepest gratitude to my advisor, Bruce Schumm, for being my mentor through undergraduate and on into my graduate career. It has been a long and arduous journey and I could not have made it to where I am today without your support. You stuck with me through thick and thin and for that I am eternally grateful. I would also like to extend my thanks to my thesis committee, Hartmut Sadrozinski and Robert Johnson, for seeing me through this adventure to the very end. You pushed me to always delve deeper and leave no stone unturned (regardless of any imminent deadlines). I am sure to carry these experiences on with me into my future work.

To Simone Mazza, Max Wilder, Forest Martinez-Mckinney, and Zach Galloway, thank you for all the mentorship you provided me in the lab. Whether I had questions about the science behind the experiments or the about the equipment running the experiments, you were always happy to help. Working hands on in the lab has always been my favorite part about doing research and it was a pleasure getting to work with you all.

I definitely could not have made it through this program without the help of Ben Miller and Amy Radovan. As the physics graduate advisors, you never missed a beat when it came to all of the little administrative tasks that always seemed to pop up. Even when I was less active on my emails than I should have been, you always found a way to get through and kick me into gear. You always had my best interests in mind and your support was an invaluable asset to me.

Lexi Daoussis and Ashton Paulus, thank you for being such incredible friends. Your encouragement, support, and understanding throughout this adventure were unparalleled. Whether through late night phone calls or motivational text messages, you were always there to help keep me going.

Franny Hamkins-Indik, you know better than anyone at this point the struggles I have with writing. Thank you for all the hours spent helping me edit and revise my thesis. I do not know what I would have done without your help.

Finally I would like to thank my family. Thank you Mom and Dad for all the love and support throughout this adventure. I cannot believe it is finally coming to an end. Grandma and Grandpa, thank you for providing me with a place to live these last six months. Being able to focus on finishing my degree without having to worry about finding housing was incredibly helpful and for that I am very grateful.

1 Introduction

Over the years, there has been a long standing challenge to provide precise timing measurements for particle physics detectors. Precise timing can be used to measure the speed of particles coming from high energy collisions which can be used to estimate the particle's mass and thus identify the type of particle [12]. Lately, experiments at the Large Hadron Collider (LHC) have been exploring the use of precise timing to separate the different collision points of each beam crossing. When the LHC is upgraded, it is expected that each crossing of the beam will have as many as 200 individual collisions [3], [4]. The density of these events will be so great that with the current spatial resolution for CMS and ATLAS, 10-20% of vertices will be composed of two events occurring so close to each other in space that they will ultimately be mistaken as a single event. It has been shown [3] that providing an accurate timing measurement of tracks emanating from these collisions can allow these vertices to be separated from each other, reducing the degradation of important signals in the detector that would otherwise occur. To achieve this goal, timing resolution of 10s of picoseconds is required.

The issue of timing with silicon diode detectors was first explored by Helmuth Spieler in the 1980s. At that time, the timing resolution achievable with silicon detectors was dominated by the effect of electronic noise, which leads to a jitter in the time at which the signal crosses a set threshold. The timing jitter of a silicon detector is given by [10], [11]

$$\sigma_j = \frac{\sigma_n}{dV/dt} \approx \frac{t_r}{S/N} \tag{1}$$

where S is the maximum pulse amplitude, t_r is the rise time of the signal, and N is the RMS readout noise. A plot of expected timing resolution versus signal-to-noise from the 1982 reference [10] is shown in Figure 1, for a rise time of 1.2 ns (the rise time readily achievable with the electronics of the day).

At that time, silicon diode sensors being developed for precision tracking had a signal-to-noise of order 10:1, leading to a timing jitter of approximately 250ps, falling short of the requirements for timing resolution discussed above. From Eq. 1, it is clear that in order to improve timing resolution, sensors must be developed with a short rise time and a high signal-to-noise ratio. The motivation behind the development of Low Gain Avalanche Detectors (LGADs) is that engineering silicon diode sensors to be thin and incorporate internal gain could lead to improvements in rise time and signal-to-noise that would allow for a significant improvement in the timing resolution. In this thesis, the properties of one version of an LGAD, (the AC-LGAD) which offers the prospect of both precise timing and position resolution in a single device, will be explored.

The Low Gain Avalanche Detector (LGAD) was first developed in the mid-2010s [6] and was enabled by advanced process controls that allow for the design of sensors with precisely controlled doping levels. The LGAD distinguishes itself from a traditional n-on-p silicon sensor by the addition of an extra p^+ implant, known as the gain layer, below the n^{++} implant. In reverse bias conditions, the gain layer generates a precisely tuned electric field in the vicinity of the n-p junction which allows for the

multiplication of signal electrons to occur, while being too low to induce significant hole multiplication. This allows for the increase of signal output of the sensor by a gain factor of 10-50, while avoiding large leakage currents.

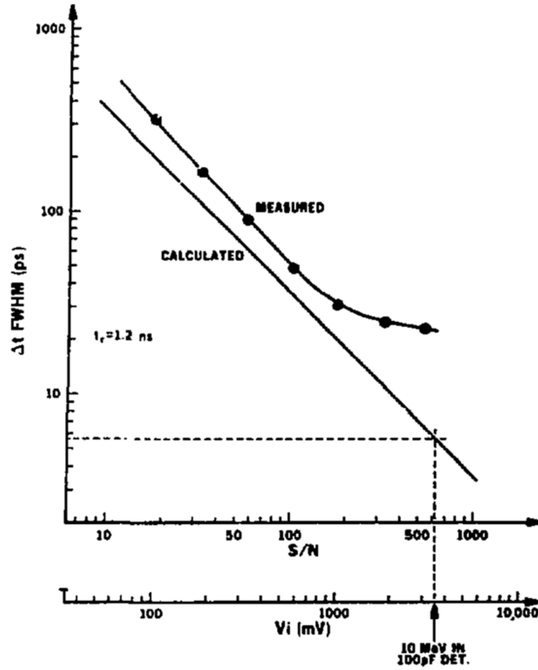

Figure 1.1. Plot of FWHM timing resolution vs. signal to noise ratio from [10]. Silicon diode detectors of the time had a signal-noise-ratio of order 10:1, giving a timing jitter of approximately 250ps, falling short of the requirements of today's detectors.

Although internal gain plays an instrumental role in improving the timing resolution of silicon sensors, it is evident from Eq. 1 that a short rise time is also needed for optimum timing resolution. As demonstrated in Appendices A.1 and A.3, the Shockley-Ramo Theorem [7], [9] can be used to show that the maximum amplitude of the current signal in a silicon sensor depends only on gain, not sensor thickness. However, the Shockley-Ramo Theorem can also be used to show that for a fixed gain, the slew rate of a silicon sensor depends only on sensor thickness, in fact, it is inversely proportional to sensor thickness. This is demonstrated in Appendix A.2. Therefore, the

next step in optimizing LGADs for timing is to decrease their rise time by making them thin. LGADs in use today typically have a thickness of order 50μm. Running with a gain of 10-20, these devices can achieve a timing resolution of order 20ps [2], [8].

Although LGADs being developed for initial applications at the upgraded LHC are capable of making very precise timing measurements, the next generation of particle detectors will require even greater spatial granularity than what was previously possible. In pixelated DC-coupled LGADs, the segmented electrodes require the addition of extra implants. The first of these is the Junction Termination Extension (JTE), which prevents early breakdown at the edges of the gain layer for each pixel. The second is the p-stop which is inserted between the JTEs for each neighboring pixel, and electrically isolates neighboring pixels on the surface to prevent short circuiting. These additional implants, and the gap between gain layers that they require, create a dead area on the sensor where charge cannot be multiplied. This dead area ultimately results in a loss of efficiency in the sensor's track reconstruction capabilities. This dead area is typically 50-100μm wide, limiting the granularity scale of conventional LGADs to the millimeter scale.

Taking advantage of the technological advancements made with LGADs, a new type of sensor was designed that utilizes the timing capabilities of LGADs but improves upon their ability to make precise spatial measurements. This sensor is known as the AC-coupled LGAD, or AC-LGAD. AC-LGADs, like standard LGADs, incorporate an internal gain layer between the n-type implant and p-type bulk. What sets them apart, however, is that between the n-type implant and readout electrodes, there is a thin

dielectric layer which AC-couples the signal to the electrodes on the surface of the dielectric. This allows for the implementation of a continuous, planar, n-type implant and gain layer throughout the sensor - rather than pixelating the gain-producing diode junction, the pixelation is established solely by the electrode pattern on the surface of the dielectric. Thus the gain layer segmentation used for standard LGADs is eliminated, resulting in a sensor with a 100% fill-factor, irrespective of the pixelation scale.

Another important distinction between AC-LGADs and standard LGADs is that the doping concentration in the n-type implant is reduced, ie $n^{++} \rightarrow n^{+}$, making it resistive. The reduction in n^{+} concentration is necessary to ensure proper signal formation in the pads, for if the doping concentration remained the same as that in a standard LGAD, the charge would be collected by the n^{++}'s DC contact before a signal had a chance to form on the AC readout pad. For this reason, AC-LGADs are also known as Resistive Silicon Detectors (RSD) and the names may be used interchangeably. AC-LGADs benefit from all of the timing achievements made with LGADs while at the same time bringing new potential for increased spatial granularity. For this reason, they promise to extend the range of possible applications in future particle physics research environments where high precision timing and position tracking capabilities are required.

In this thesis, several different AC-LGAD fabrication configurations were examined in hopes of providing guidance towards the further development and optimization of AC-LGADs. Each sensor had the same pad geometry, a 3x3 array of 200μmx200μm pads with a 500μm pitch. The parameters that varied between sensors

were the n^+ concentration and the thickness of the dielectric layer. In each experiment, only a single parameter was changed at a time. The sensors were characterized using the Transient Current Technique (TCT). Signal was generated using an IR laser, λ=1064nm, which illuminated the front side of the sensor, generating charges through ionization. Because IR light has an attenuation length of approximately 1000µm and the sensors studied in this thesis had a bulk thickness of 50µm, charges were generated nearly uniformly throughout the bulk of the sensor. These charges then undergo multiplication as they drift towards their respective electrodes. The laser's intensity was set such that the resulting ionization would approximate that of a minimum ionizing particle (MIP).

This study had four main objectives. The first was to make a qualitative examination of how changing the n^+ concentration and dielectric thickness affected the shape of the RC fall off, or undershoot, of the AC signal. Next was to examine how the pulse arrival time changed as a function of the energy deposition's distance from the readout pad and how this change was affected by the n^+ concentration and dielectric thickness of the sensors. The third and fourth were to study the effects of changing n^+ concentration and dielectric thickness on the position and timing resolutions of AC-LGADs.

2 Apparatus

2.1 Sensors

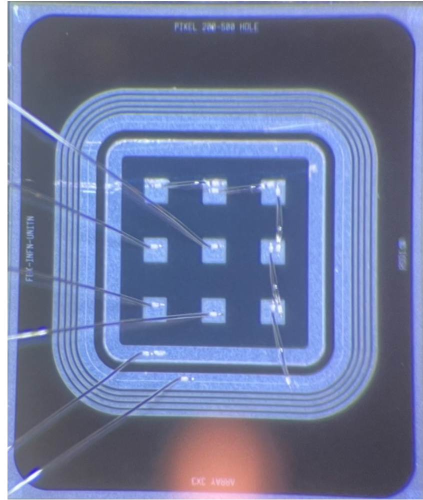

Figure 2.1. Image of sensor geometry studied. 3x3 array of 200µm square pads with a 500µm pitch. Four pads were wire bonded to the readout electronics while the rest were connected to ground.

For the following experiments, a single sensor geometry was used. Each sensor was made up of a 3x3 array of square pads which were 200µm wide and had a pitch of 500µm. This can be seen above in Figure 2.1. Table 1 shows the fabrication parameters for various different AC-LGAD wafers made by Fondazione Bruno Kessler (FBK). The wafers used in the following experiments were wafers 3, 4, 8 and 13. Wafers 3, 8, and 13 differ only in their n^+ concentration, A, B, and C, respectively. The n^+ dose labeled B is 1/10th the dose of a standard LGAD, A is half the value of B, and C is twice the value of B [5]. Wafers 3 and 4, on the other hand, have the same n^+ dose but differ in their dielectric thickness. Unlike with the n^+ doses, no quantitative value was given for the dielectric thicknesses, only that they were "implemented in two

configurations, low (L) and high (H), by slightly changing the growth thickness during the deposition process . . .” [5].

Split table (with breakdown voltage)						
wafer	*n* -plus dose	*p* -gain dose	dielectric thickness	*p* -stop dose	substrate	Vbd
1	A	0.92	L	B	Si-Si	480
2	A	0.94	L	A	Si-Si	440
3	A	0.94	L	B	Epi	460
4	A	0.94	H	B	Si-Si	440
6	B	0.92	L	B	Epi	525
7	B	0.94	L	A	Si-Si	460
8	B	0.94	L	B	Si-Si	460
10	B	0.96	H	B	Si-Si	430
11	C	0.92	L	B	Si-Si	515
12	C	0.94	L	B	Epi	490
13	C	0.94	L	B	Si-Si	465
15	C	0.96	H	C	Si-Si	445

Table 1. Fabrication parameters for different wafers of AC-LGADs made by FBK. Wafers studied in these experiments were 3, 4, 8, and 13.

2.2 Readout

All four sensors were mounted on a single 16 channel amplifier board designed at Fermilab. The amplifier’s readout electronics were then wire bonded to the pads of each sensor. Four of the nine pads were bonded to the readout electronics. The remaining five pads were connected to ground. This is seen in Figure 2.2 below and Figure 2.1 above. The amplifier board with mounted sensors was placed inside the TCT laser housing on a three axis stage where the sensors were biased and illuminated with an IR laser. The sensors were biased with a Keithley 2410 Source Measure Unit (SMU) and the bias was set such that the resulting pulse height near the edge of the pad was about 150mV. The laser intensity was set such that the amount of ionization induced would replicate that of a MIP passing through. The laser signal was split, sending half to the sensor and the other half to a reference diode. This diode was used to monitor

the intensity of the laser throughout each experiment and correct for fluctuations in the sensor's signal due to the temperature fluctuations of the laser.

The amplifier used on the Fermilab board was a fast two stage amplifier with a 1GHz bandwidth. Signal was read out using a Tektronix DPO 7254 (2.5GHz, 40GS/s) oscilloscope which was triggered directly by the laser. Signal was read out from the center pad of each sensor to provide the largest area of signal collection.

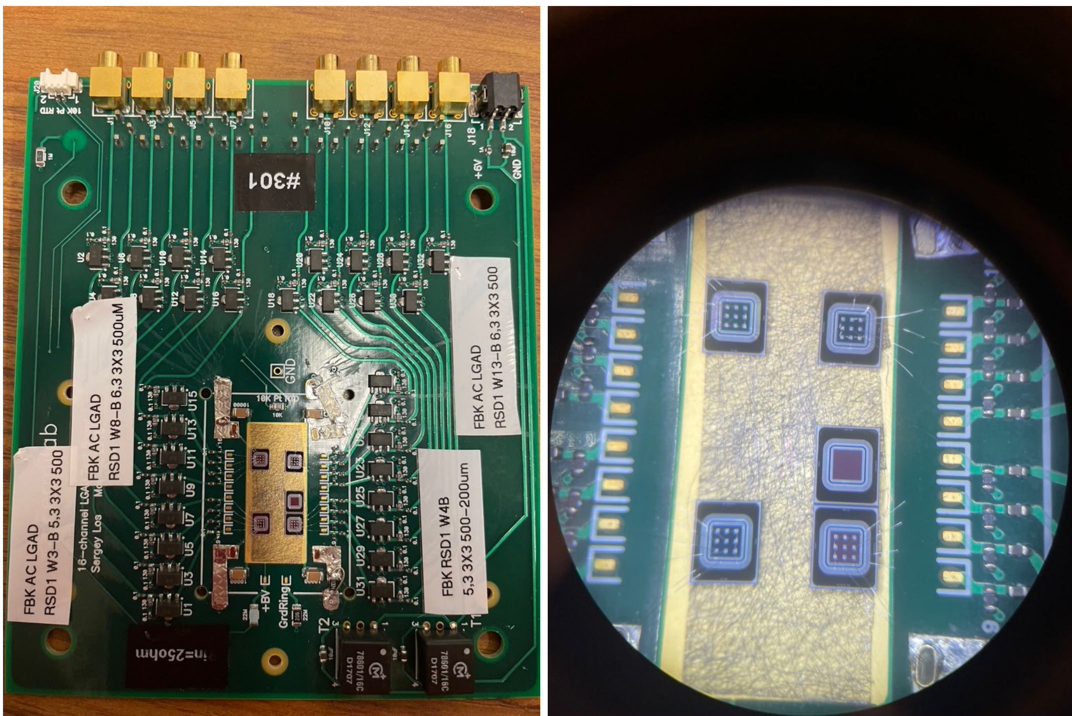

Figure 2.2. (Left) Fermilab 16 channel amplifier board with all four AC-LGAD wafers mounted. (Right) Microscope picture of mounted sensors on amplifier board.

3 Procedure

The following procedure was applied for all studies conducted. After mounting the amplifier board in the TCT laser housing and biasing the sensor, the laser performed a scan that spanned the center pad and its surrounding area (820µmx820µm) using 10µm steps. The area was set such that the scan would reach edges of the surrounding pads. In each position, the average of 100 waveforms was recorded. A 100 waveform average was chosen because it served as a compromise between noise reduction and maintaining a reasonable acquisition time. Averaging over 100 waveforms gave an RMS noise of about 0.2mV, yielding clear resolution of the pulses. Information extracted from these waveforms was used to calculate the position and timing resolutions of each wafer. An example of a scan is shown in Figure 3.1 below where maximum pulse height is plotted as a function of position. The red arrow shown in Figure 3.1 represents the location of the projections used in the position and timing resolution analyses and will be discussed in Section 4.

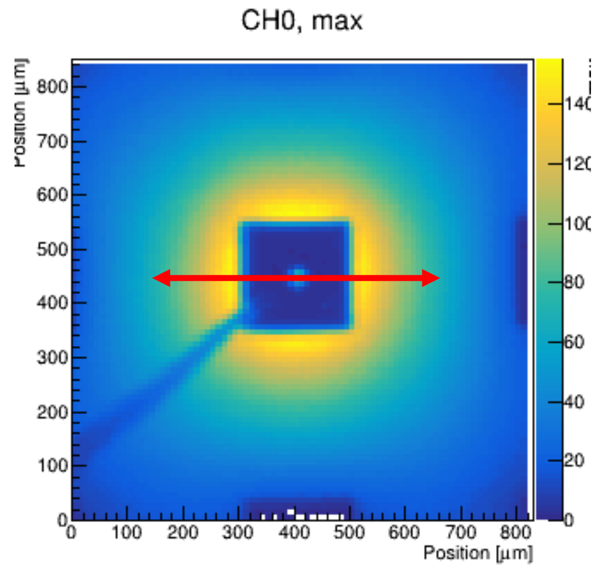

Figure 3.1. Sample scan of maximum pulse heights. The laser scanned an 820µmx820µm area around the center pad in 10µm steps. Average pulses were recorded in each location. The information extracted from these pulses was used to characterize the different wafers. The red arrow represents the location of the projections used in the Section 4 analyses.

4 Results and Analysis

4.1 Pulse Comparison Between Wafers

It is helpful to begin the analysis by looking at the shape of the signal pulses for the various sensors to get a qualitative idea of how the different n^+ doses and dielectric thicknesses affect the charge collection process. Each pulse begins with a positive first lobe resulting from the arrival of the gain electrons to the n^+ layer. As they discharge to ground through the n^+ layer, a second, negative, lobe is created. The resistive n^+ layer and capacitive dielectric layer make an effective RC circuit in the readout path. The discharge of the second negative lobe has a time constant given by the RC of this circuit. The sheet resistance of a sensor depends on the n^+ concentration; a lower n^+ concentration will result in a higher sheet resistance and vice versa. The capacitance of a sensor, on the other hand, depends on the dielectric thickness. A thinner dielectric layer results in a greater capacitance. Increasing R or C results in a slower drift of charge through the n^+ layer, giving the pulse undershoot a longer tail. Additionally, the AC nature of the pulses causes the total signal to integrate to zero. Therefore, for pulses with the same initial positive lobe, differences in the second, negative, lobe are expected based on the different R (n^+) and C (dielectric thickness) parameters of each sensor.

It is also important to note that the undershoot of the pulse is influenced by the type of amplifier used. For a given amplifier, differences in wafers can be expected based on the fabrication parameters of the wafers; however, the same sensor may

exhibit different behaviors using different types of amplifiers. In a separate study, a single sensor was examined first using the 16 channel Fermilab board used in this thesis and later using a faster single channel amplifier developed at the Santa Cruz Institute for Particle Physics (SCIPP). It was found that the leading edge of both pulses was the same for both amplifiers, showing that the rise time was indeed a characteristic of the sensor rather than of the amplifier. Where the two signals differed was in the time it took for the signal peak to fall and in the depth of the undershoot. The SCIPP board showed a shorter fall time and a deeper undershoot than that of the Fermilab board, representing a "truer" depiction of the signal shape within the sensor. However, it was found that the RC discharge of the pulses on both amplifier boards realigned with one another, showing that the time constant, RC, is also an intrinsic characteristic of the sensor.

Pulses were examined for three distinct locations of the laser beam on the sensor: near the edge of the center pad, near the midway point between the center pad and the left adjacent pad, and near the edge of the left adjacent pad. These positions are represented by the red dots in Figure 4.1. In all cases, the center pad is the readout electrode producing the observed signal. To examine how changing the n^+ concentration and dielectric thickness affected the shape of the pulses in each of these locations, the pulses were first normalized and aligned in time. A constant scale factor, unique to each wafer, was used to normalize the pulses. The scale factor was chosen such that it would set the maximum pulse height of the near edge pulses to be 150mV. The scale factors for wafers 3, 8, and 13 reduced their maximum signal height by 1-

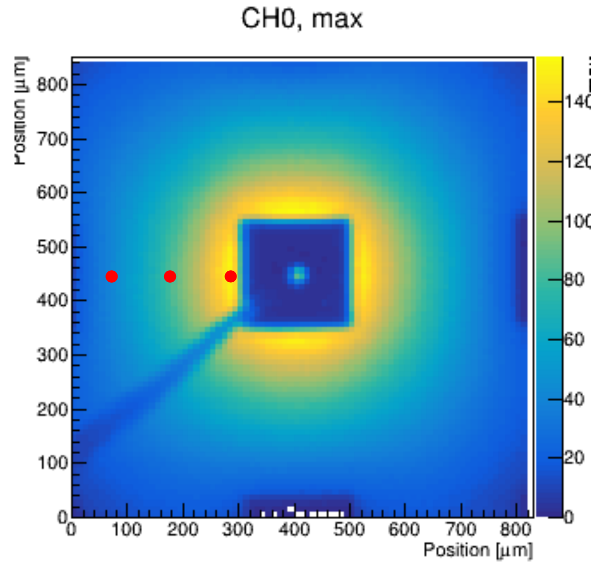

Figure 4.1. Red dots represent the locations used to examine average pulse shapes. Pulses were examined near the edge of the center pad, near the midpoint between the center pad and the left adjacent pad, and near the edge of the left adjacent pad.

4%, depending on wafer, to match 150mV. Wafer 4 was not normalized by eye as well as the other three and required an approximately 13% increase to match 150mV. As mentioned in Section 2.2, this was done in order to replicate the signal of a MIP.

4.1.1 Pulse Shape n^+ Comparison

This section will examine how varying the n^+ concentration from wafer to wafer affects the charge collection process in AC-LGADs, namely how the shape of the RC undershoot changes as a function of n^+ concentration. The wafers studied in this experiment were wafers 3, 8, and 13. Referring back to Table 1, W3 has the lowest n^+ concentration, followed by W8, then W13. The n^+ concentration of W3 is half the n^+ concentration of W8 and the n^+ concentration of W13 is twice the n^+ concentration of W8. Due to the inverse relationship between n^+ concentration and sheet resistance this amounts to W3 having the greatest sheet resistance, followed by W8, then W13.

The normalized pulses for wafers 3, 8, and 13 are shown in Figure 4.2: near the edge of the center pad (a), between the center pad and the left adjacent pad (b), and near the edge of the left adjacent pad (c). In Figure 4.2(a), the initial positive pulses are nearly identical for all three wafers; this is due to the normalization described above. The RC undershoots, on the other hand, are different from wafer to wafer. Figures 4.2(b) and 4.2(c) show that although the maximum pulse heights of the different wafers die out at different rates moving away from the pad, a roughly constant rise time is still observed.

To better investigate the effects of n^+ concentration on the shape of the undershoots, the pulses from Figure 4.2 were zoomed in to show just the undershoots. This is shown in Figure 4.3 below. It is clear that the undershoot of W13 has the greatest magnitude as well as the quickest return to baseline. After W13, the undershoot of W8 has the second largest magnitude and the second fastest return to baseline. Finally, the undershoot of W3 has the smallest magnitude and the slowest return to baseline. The results show that as n^+ concentration is increased, the magnitude of the undershoot is increased. Additionally, as n^+ concentration is increased the return to baseline time is decreased. Modeling the discharge of the undershoots as an AC circuit with a time constant equal to RC, where R is the sheet resistance of the n^+ layer and C is the capacitance of the dielectric layer, these results match what is expected. By increasing the n^+ concentration and thus decreasing the resistance, a smaller time constant is observed.

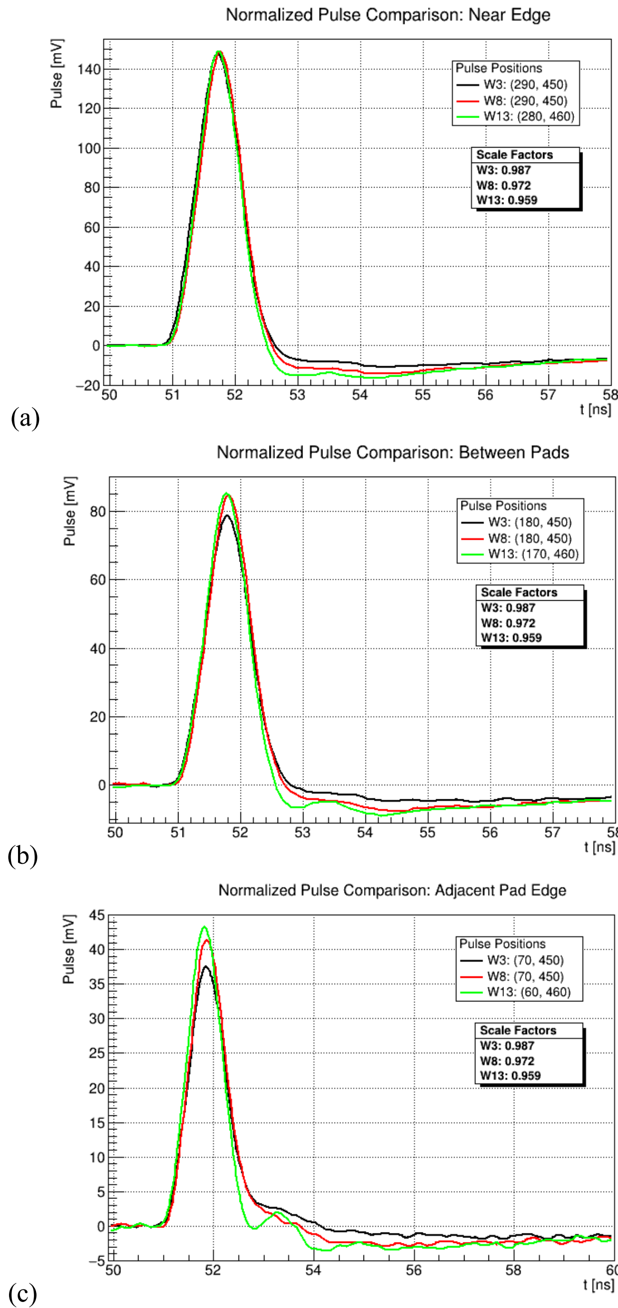

Figure 4.2. Normalized pulses for wafers 3, 8, and 13. Plots (a), (b), and (c) correspond to locations on the sensor near the edge of the center pad, between the center pad and the left adjacent pad, and near the edge of the left adjacent pad, respectively, as shown in Figure 4.1. (a) shows that when normalized, each wafer has a nearly identical initial positive pulse. The RC undershoots, however, vary significantly between wafers. (b) and (c) show that although the signal dies out at different rates between wafers, a constant rise time is still observed among the three. A clear separation between the undershoots is still observed.

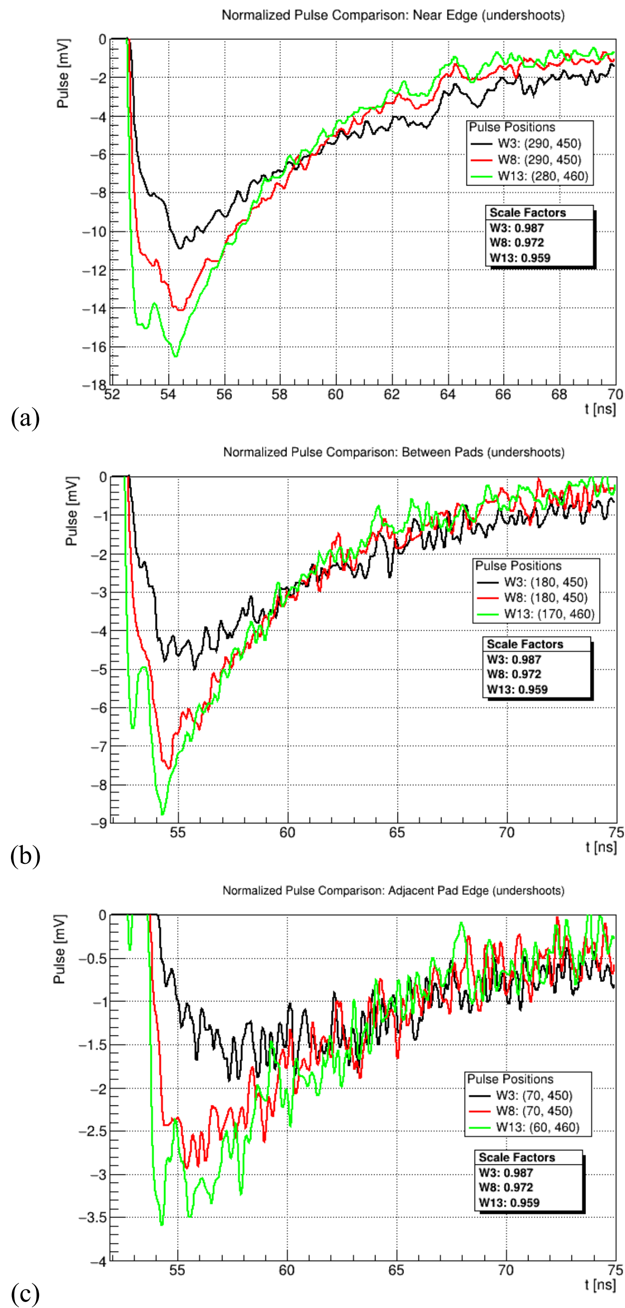

Figure 4.3. Undershoots of normalized pulses shown in Figure 4.2. In each location W13 (green) has the greatest magnitude of undershoot as well as the shortest return to baseline time followed by W8 (red), then W3 (black). The data show a clear correspondence between undershoot shape and n^+ concentration.

4.1.2 Pulse Shape Dielectric Thickness Comparison

In this section, the effects due to changing the thickness of the dielectric AC-coupling layer on the pulse shapes will be examined. In this experiment, the wafers studied were wafers 3 and 4. Wafer 3 has a "low" dielectric thickness and W4 has a "high" dielectric thickness according to Table 1. As stated in Section 2.1, low and high have not been given any quantitative value, just that the growth thickness was slightly changed between the two. This means that W3 has a greater capacitance between the n^+ layer and readout pad than W4 due to its thinner dielectric layer.

Figure 4.4 shows the normalized pulses for wafers 3 and 4 near the edge of the center pad (a), between the center pad and an adjacent pad (b), and near the edge of the adjacent pad to the left (c). Figure 4.4(a) shows that near the edge of the center pad, the initial pulses are nearly identical for both wafers but have different undershoots due to their differing capacitances. Figures 4.4(b) and 4.4(c) further affirm that rise time remains roughly constant regardless of pulse height or position between the pads. Like in the N+ comparison, the effects of varying the dielectric thickness on the shape of the undershoots were further examined by plotting only the undershoots from the pulses in Figure 4.4. This is shown in Figure 4.5.

It is clear, looking at Figure 4.5, that the undershoots of W4 have the greatest magnitude as well as the quickest return to baseline. Recall that W4 has a thicker dielectric layer, and thus a greater capacitance than W3. The results ultimately show that as the dielectric thickness is increased, or capacitance decreased, the magnitude of the undershoot increases and its return to baseline time decreases. Modeling the

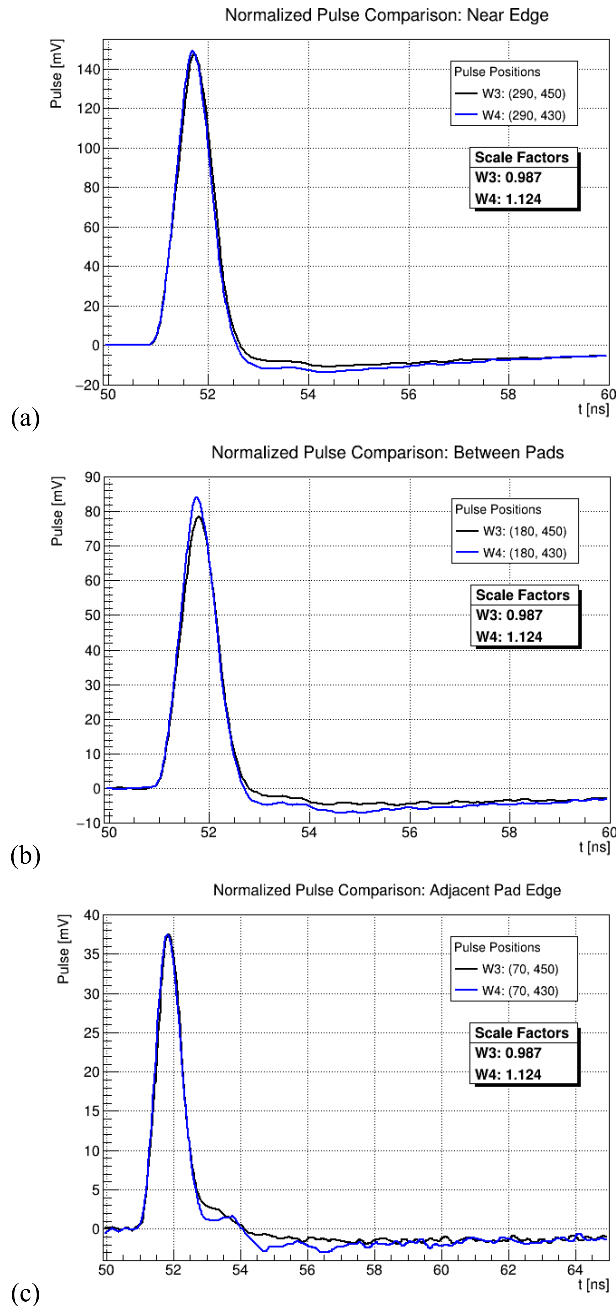

Figure 4.4. Normalized pulses for wafers 3 and 4. Plots (a), (b), and (c) correspond to locations on the sensor near the edge of the center pad, between the center pad and the left adjacent pad, and near the edge of the left adjacent pad, respectively, as shown in Figure 4.1. (a) shows that when normalized, each wafer has a nearly identical initial positive pulse. The RC undershoots, however, vary significantly between wafers. (b) and (c) show that although the signal dies out at different rates between wafers, a constant rise time is still observed among the two. A clear separation between the undershoots is still observed.

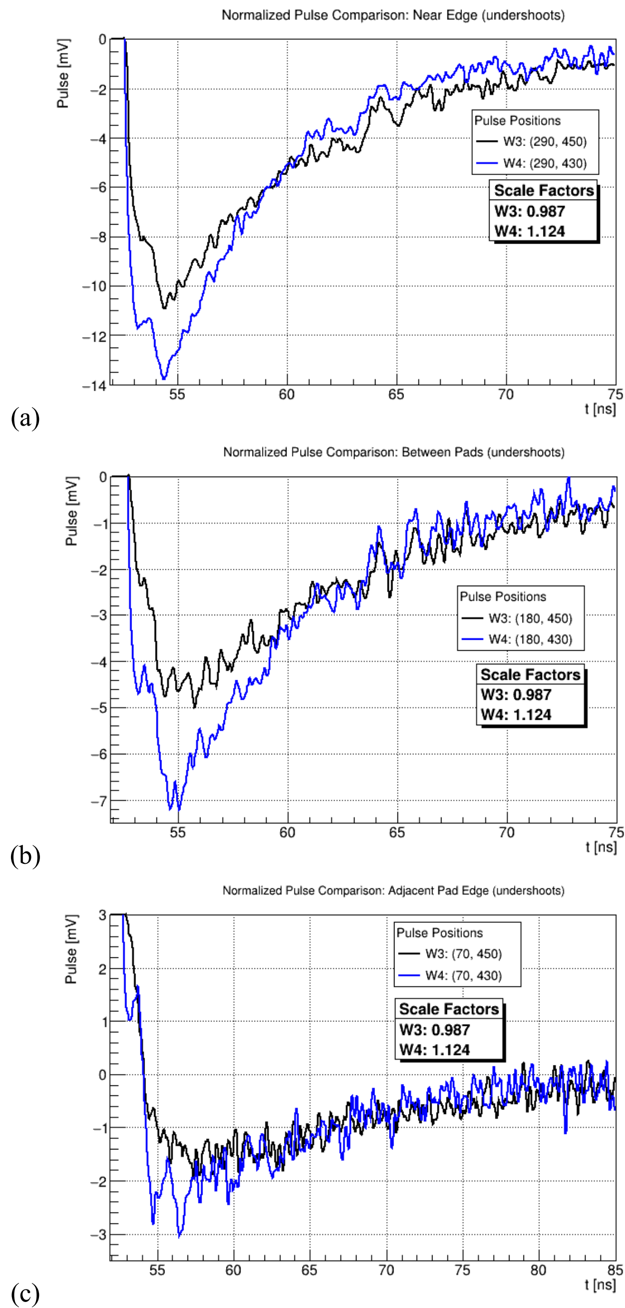

Figure 4.5. Undershoots of normalized pulses shown in Figure 4.4. In each location, W4 (blue) has a greater magnitude of undershoot as well as a shorter return to baseline time. Wafer 4 has the greater dielectric thickness of the two. With the other fabrication parameters held constant, the data show a clear correspondence between dielectric thickness and undershoot shape.

discharge of the undershoots as an AC circuit with a time constant of RC, these results also match what is expected. Wafer 4 with the thicker dielectric layer and thus smaller capacitance, shows a smaller time constant than W3.

4.1.3 Summary of Results for Pulse Comparisons

This study examined how changing the n^+ concentration and dielectric thickness affected the shapes of the RC undershoots of AC-LGAD signal pulses. The discharge of the pulse undershoots thus far has been modeled by an RC circuit where R is the sheet resistance of the n^+ layer and C is the capacitance of the dielectric AC-coupling layer. In this model, the undershoots are expected to discharge with a time constant given by RC. Using this information, it was expected that sensors with a lower sheet resistance or capacitance would discharge faster.

The n^+ comparison showed that as n^+ concentration was increased, the magnitude of the undershoot was increased and the time it took for the signal to return to baseline was decreased. Wafer 13, which had the greatest n^+ and thus lowest sheet resistance, had the quickest return to baseline, followed by W8, then W3. The dielectric thickness comparison showed that as dielectric thickness was increased, the magnitude of the undershoot was increased and the time it took for the signal to return to baseline was decreased. Wafer 4, with the thicker dielectric layer and thus lower capacitance, had a quicker return to baseline than W3. Both experiments matched expectations. Whether by n^+ concentration or by dielectric thickness, decreasing R or C resulted in a smaller observed time constant for each of the pulses studied.

4.2 Pulse Delay Comparison

In addition to comparing the pulse shapes of the different wafers, the pulse arrival time, or delay, t_d, was also examined. The delay in these studies is defined as the time it takes, after receiving a trigger from the laser, for the leading edge of the signal pulse to reach 50% of the maximum pulse height. Because the overall magnitude of the delay is determined primarily by the length of the signal path through the readout electronics, the important characteristic to compare between wafers is not the delay itself, but the rate of change of delay with position.

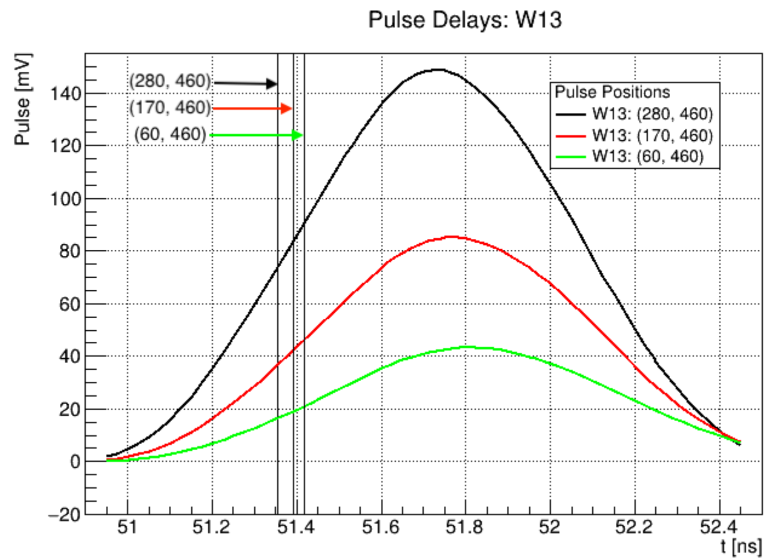

Figure 4.6. Overlay of pulses from the locations shown in Figure 4.1. Vertical lines represent the time at which the signal height reaches 50% the maximum pulse height (the delay). The delay is seen to increase as distance from the readout pad increases.

To characterize the effects of varying n^+ concentration and dielectric thickness on the rate of change of delay with position, the delay of each wafer was measured as a function of position. Figure 4.6 shows an overlay of pulses for W13 from each of the locations shown in Figure 4.1. The vertical lines mark the time, t_d, for each location,

where the signal has reached 50% of its maximum height. They show that as the location of the energy deposition moves further from the edge of the pad, the delay increases. The data from each wafer showed that the delay had a roughly linear dependence on position. Accordingly, the data were fit to a line. The resulting slopes are given in Table 2. It was found that as n^+ concentration increased (sheet resistance decreased), the rate of change of delay with position decreased. The data also showed that as dielectric thickness decreased (capacitance increased) the rate of change of delay decreased. Depending on wafer, the rate of change of delay ranged from 0.28-0.47ps/µm. A rate of change of 0.3ps/µm at a distance of 200µm results in a delay of 60ps. This value is greater than the current temporal resolution of standard DC-coupled LGADs. Therefore, to fully utilize AC-LGADs for precision timing measurements, a correction must be made to account for the increase in delay that comes with increased distance from the readout pad.

Pulse Delay Fit Results

Wafer	Rate of Change of Delay (ps/µm)
3	.41
8	.32
13	.28
4	.47

Table 2. Pulse delay fit results. Increasing n^+ concentration decreases rate of change of delay. Decreasing dielectric thickness decreases rate of change of delay.

4.3 Position Resolution

Position resolution is a critical characteristic of AC-LGAD performance. Making use of the natural charge sharing between neighboring channels, the position of the passing particle can be estimated by observing what the relative amounts of charge in each channel are. With charge sharing, the position of the passing particle can be determined to much better precision than the size of the pixel divided by $\sqrt{12}$, which is the resolution one would obtain if there were no charge sharing. This allows for a precise determination of the position for a relatively large pixel size, meaning that the sensor can have fewer channels, leading to a simplified design.

In this study, only the determination of the position for particles passing through the area between two pads was considered. For a particle passing through the region below a given pad, the position can be approximated as being in the center of the pad, with a position resolution given by $\frac{p}{\sqrt{12}}$, where p is the pad width. To the extent that there is charge sharing between neighboring channels for particles passing directly underneath pads, this can be improved, but such an approach is not considered in this thesis.

In understanding how to calculate position resolution, a fraction parameter, F, can be defined according to the following:

$$F(x)_i = \frac{P_{max}(x)_i}{Sum(x)} \tag{2}$$

where $P_{max}(x)_i$ is the maximum pulse height of pad i, $Sum(x)$ is the total signal from each of the pads being read out, and x itself is the location of the deposition

between the pads. In the case of this study, the position resolution is that associated with the determination of the position from the two neighboring pads that surround the deposition. Accordingly, $Sum(x)$ is given by the following:

$$Sum(x) = P_{max}(x)_L + P_{max}(x)_C \tag{3}$$

where L and C represent the left and center pads, respectively. The fraction parameter is a crucial component in the position reconstruction of particle hits as it is the parameter that allows you to determine the distance from a given strip or pad based on the amount of signal received: each value of the fraction, F, corresponds to a unique value of the distance parameter, x.

The faster the fraction parameter changes with respect to the distance parameter, the more precisely the position can be determined, i.e. the position resolution is proportional to $1/\frac{dF}{dx}$, the inverse of the derivative of the fraction with respect to distance. But also, the ability to determine the fraction parameter, F, is determined by the total signal-to-noise, $\frac{Sum(x)}{\sigma_n}$, where σ_n is the RMS noise. Since two channels are required in order to determine the fraction, each with RMS noise σ_n, the position resolution, σ_x, is thus given by

$$\sigma_x = \sqrt{2}\frac{dx}{dF}/(\frac{Sum}{\sigma_n}) \tag{4}$$

From Eq. 4, we find that there are two main contributors to position resolution in AC-LGADs. The first is the rate of change of P_{max} fraction with position; the greater the change in fraction with position, the better the resolution. The second is the total

signal-to-noise ratio; sensors with high gain and low noise lead to better position resolution.

The following analysis uses the P_{max} distributions from two adjacent pads to approximate the position resolution of the different wafers studied. P_{max} distributions were obtained by taking a one dimensional projection from the two dimensional scan shown in Figure 3.1. A horizontal projection passing through the center of the sensor's center pad was used. This projection is represented by the red arrow shown in Figure 3.1. The P_{max} distributions emanating from either side of the center pad were normalized independently from one another. In both cases, the distributions were multiplied by a constant scale factor, unique to each wafer, that set the value of P_{max} near the edge of the center pad to be 150mV, the signal expected from a MIP. These scale factors are given in Table 3. Because signal was only recorded on the center pad of each sensor, the translational symmetry of the distributions was used to model the P_{max} distribution of a pad adjacent to the center pad. The P_{max} distributions for wafers 3, 4, 8, and 13 are given in Figure 4.7(a). They show the distribution obtained when the central channel is read out. The cutaway region from approximately 300-500μm represents the location of the metal pad where the laser could not penetrate through to the silicon. Taking advantage of the symmetry of the pad pattern, the P_{max} distribution emanating from the right side of the center pad was translated approximately 500μm to the left, lining up the apparent edge on the latter portion of the distribution with the left edge of the center pad. The resulting effect was a simulated P_{max} distribution

coming from the adjacent pad to the left of the center pad. This is shown in Figure 4.7(b).

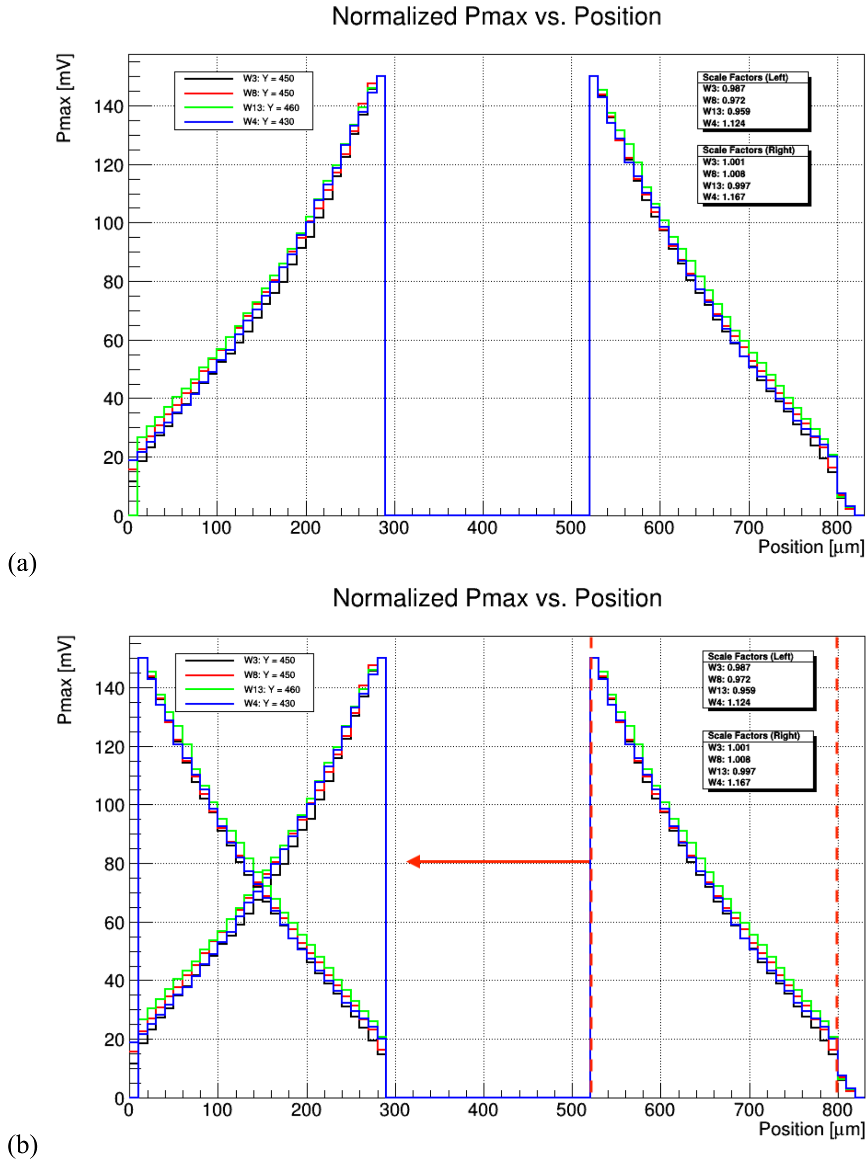

Figure 4.7. Normalized P_{max} distributions for wafers 3, 4 ,8, and 13. (a) shows the distributions projecting horizontally through the center of the center pad. The distributions on either side of the pad were normalized independently by scaling the distributions such that the value near the edge of the pad would equal 150mV. (b) shows the effect of translating the distributions on the right side of the pad over to the left, modeling a P_{max} distribution coming from the left adjacent pad. The region covered by the pad is not measured because the laser cannot penetrate the metal electrode.

Pmax Normalization Scale Factors		
Wafer	Left of pad	Right of pad
3	0.987	1.001
8	0.972	1.008
13	0.959	0.997
4	1.124	1.167

Table 3. Scale factors used to normalize P_{max} distributions. Distributions on either side of the pad were scaled such that the value near the edge of the pad would equal 150mV.

The first step in calculating the position resolution, after generating the P_{max} distribution of the second pad, was to form the quantity $Sum(x)$, the sum of the neighboring P_{max} distributions. It is important to understand how $Sum(x)$ varies from wafer to wafer because of its direct correlation to the fraction parameter, F, as is seen in Eq. 2. Figure 4.8 shows a plot of $Sum(x)$ vs. position for wafers 3, 4, 8, and 13. In the region from 0-100µm, $Sum(x)$ for wafers 3 and 4 are seen to overlap. Wafers 4 and 8 are also seen to overlap in the region from 200-300µm. Aside from those two instances of overlap, there is a distinct order between the total amount of signal produced by the wafers, even after the signals are normalized to be the same at the edge of the readout pad. In order from greatest to least the wafers are W13, W8, W4, and W3. Looking back to Table 1, W13 has the greatest n^+ concentration, followed by W8, then wafers 3 and 4 (whose n^+ doping densities are the same but vary in dielectric thickness). Accordingly, Figure 4.8 suggests that as n^+ doping density is increased, or sheet resistance is decreased, the sensor can record a greater signal as the laser, or incident particle, moves away from the pad. Figure 4.8 also suggests that increasing dielectric thickness, or decreasing capacitance, will have the same effect, allowing a greater signal to be recorded at further distances from the pad edge.

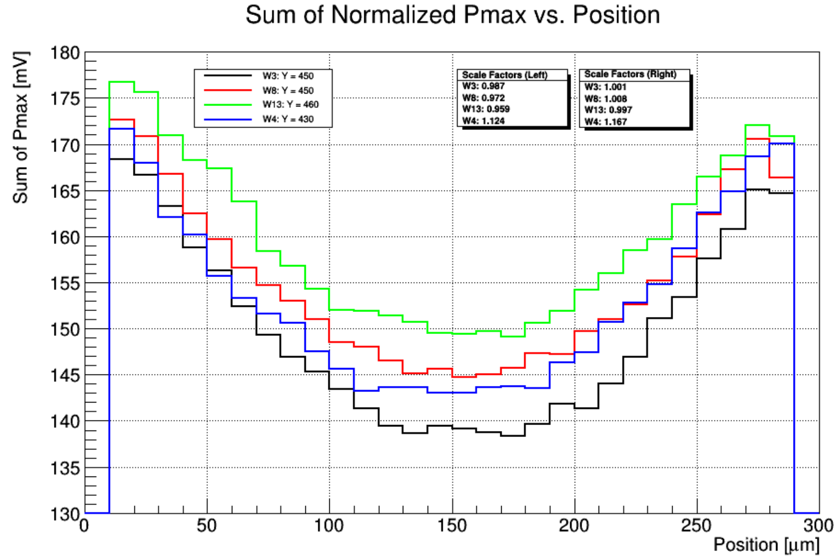

Figure 4.8. Total signal, $Sum(x)$, from two adjacent pads for wafers 3, 4, 8, and 13. Wafer 13 shows the greatest signal, followed by W8, then W4 and W3. The data suggests that as n^+ concentration is increased, or sheet resistance is decreased, $Sum(x)$ is increased. Similarly, increasing dielectric thickness, or decreasing capacitance, is shown to increase $Sum(x)$ as well.

It is important to note that $Sum(x)$ in Figure 4.8 is not constant as a function of position. This is because the sensors studied in this thesis were composed of an array of pads and charge, to some degree, is shared amongst every pad. In this configuration, signal leakage to neighboring pads is inevitable. Projections through the center of the center pad were used in the analyses of this thesis in order to mitigate the effects of leakage to the greatest extent possible. In a strip sensor, where charge is primarily shared between the two adjacent strips on either side of the deposition, one can expect to see a roughly constant $Sum(x)$ for all positions between the strips. Similarly, if one has the capability to read out all channels of an array type sensor simultaneously, then $Sum(x)$ can be expected to remain constant throughout the sensor area.

To get the total signal-to-noise ratio, the total signal distribution shown in Figure 4.8 was divided by the RMS noise of the amplifier board, 2.5mV, which is

independent of channel or wafer. This is shown in Figure 4.9. Because the value for noise in the signal-to-noise ratio was taken to be a constant, the same conclusions about the $Sum(x)$ distribution apply here. However, as shown in Eq. 4, position resolution is inversely proportional to the signal-to-noise ratio. Thus in observing how the signal-to-noise ratio changes with position, information is gained about how the position resolution is expected to change as a function of position.

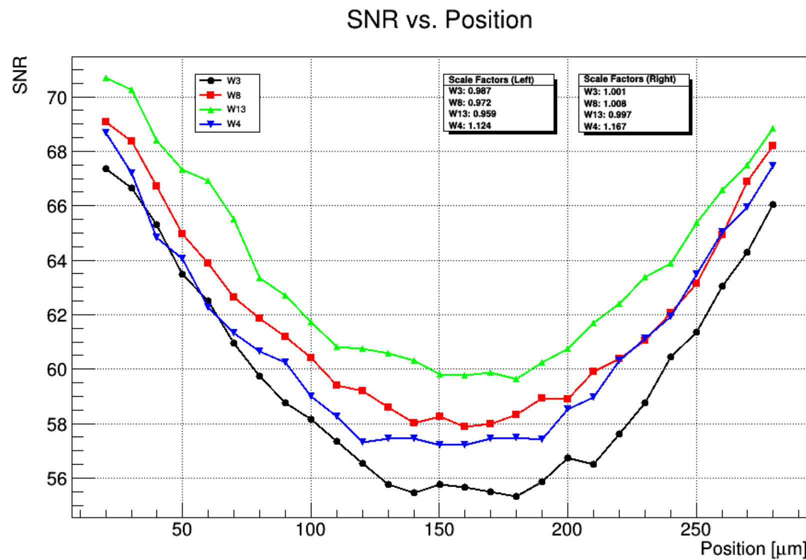

Figure 4.9. Total signal-to-noise ratio vs. Position for wafers 3, 4, 8, and 13. Signal-to-noise ranges from 55 to 71. Wafers 3 and 4 show some overlap from 0-100µm and wafers 4 and 8 show some overlap from 200-300µm. Overall, a trend is seen that as n^+ concentration is increased (sheet resistance decreased), so is signal-to-noise ratio. Wafers 3 and 4 have the same n^+ concentration but different dielectric thickness. Wafer 4 has a thicker dielectric layer (less capacitive) and is seen to have a greater signal-to-noise ratio than W3.

Figure 4.9 shows that with this experimental setup a signal-to-noise ranging from 55 to 71 is achieved. Comparing the differences in signal-to-noise ratio between wafers, the average differences were found to vary from about 2-7% depending on wafers compared. The average maximum difference in signal-to-noise ratio across all wafers was about 7%. Signal-to-noise is lowest near the midpoint between the pads and

grows as the readout pad is approached. Based on what is shown in Figure 4.9, position resolution should be most precise near the readout pads and conversely should be least precise in the center point between the pads. Based on signal-to-noise alone, it would be expected that W13 would have the most precise position resolution due to having the greatest signal-to-noise ratio. Conversely, W3 would have the least precise position resolution due to having the lowest signal-to-noise ratio.

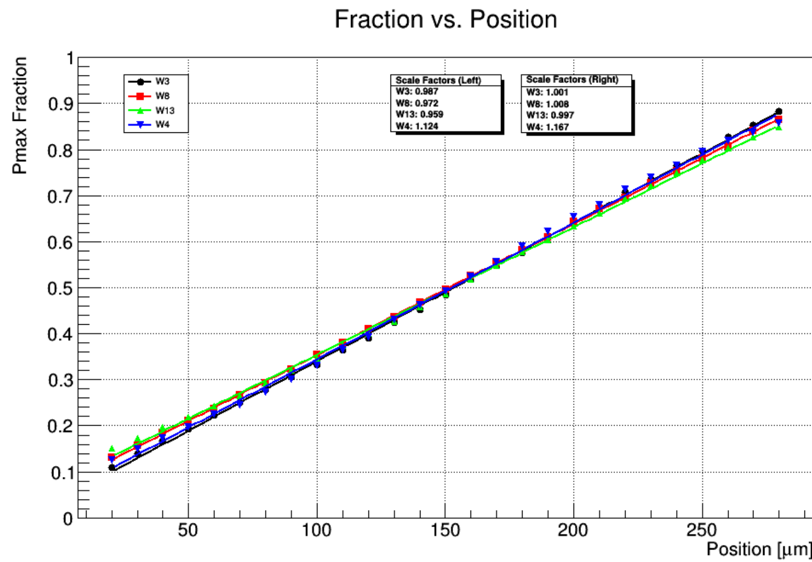

Figure 4.10. P_{max} Fraction vs. Position for wafers 3, 4, 8, and 13. Fraction shows a roughly linear dependence on position.

After gaining an understanding of how $Sum(x)$ behaved as a function of position for each wafer, the P_{max} and $Sum(x)$ distributions were used to calculate the fraction parameter, F, which is plotted against position in Figure 4.10. In order to calculate the position resolutions of the different wafers, the plots in Figure 4.10 were inverted and fit to a line, which is shown in Figure 4.11. The slopes resulting from these fits are given in Table 4. Figure 4.11(a) shows the entire distribution between the pads,

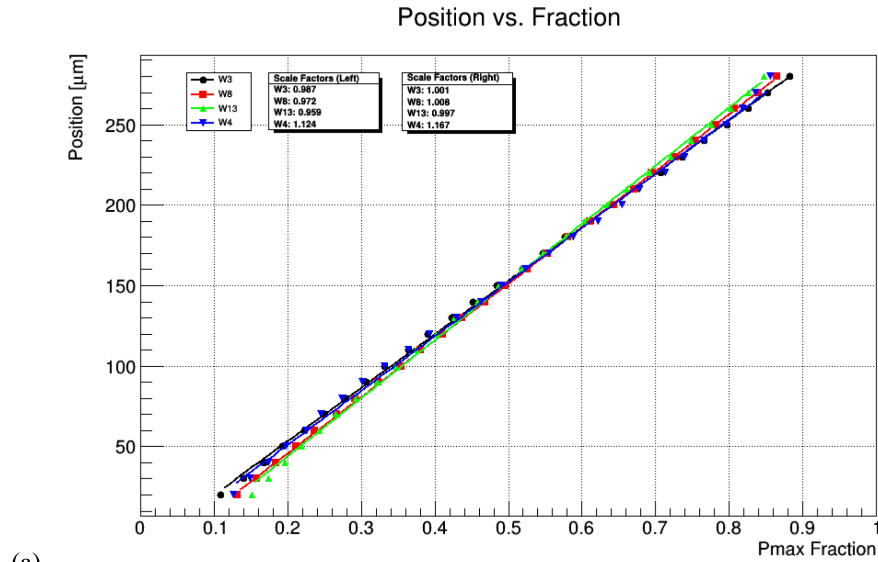

(a)

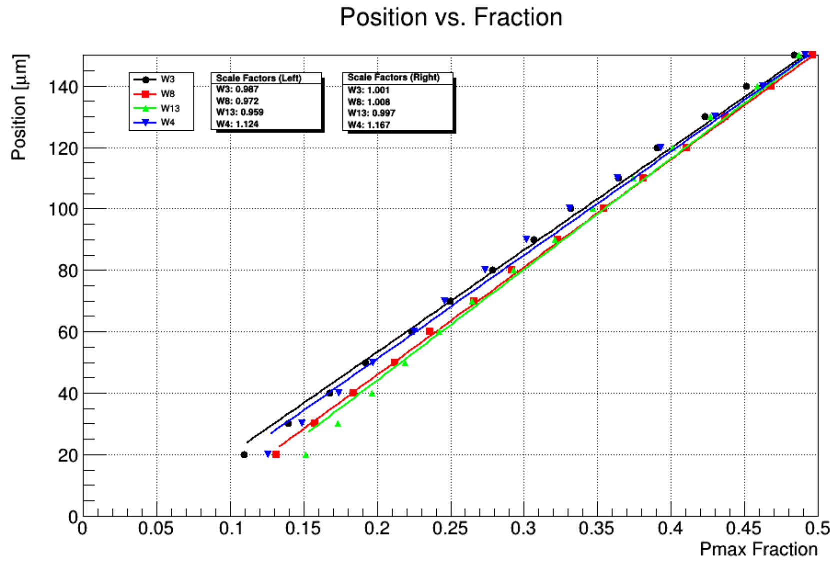

(b)

Figure 4.11. Position vs. P_{max} Fraction distribution for wafers 3, 4, 8, and 13. (a) shows the entire distribution between pads. Each data set was fitted to a line and the resulting slopes were used in Eq. 4 to calculate the position resolutions of each wafer. Position resolution is directly proportional to $\frac{dx}{dF}$, so a steeper slope results in a worse resolution. (b) shows a zoomed in plot of (a) to better illustrate the differences between wafers. Wafer 13 shows the greatest slope, followed by W8, W4, then W3. The data show a trend that as n^+ concentration is increased, $\frac{dx}{dF}$ is increased. Wafer 4 has a steeper slope than W3, suggesting that as dielectric thickness is increased, $\frac{dx}{dF}$ is increased.

while Figure 4.11(b) zooms in to better show the differences between wafers. The data show W13 as having the greatest slope, followed by W8, W4, and W3. Comparing the

slope values given in Table 4, differences in $\frac{dx}{dF}$ between wafers range from approximately 2-9%. Recall from Eq. 4 that position resolution is directly proportional to $\frac{dx}{dF}$. Therefore, the smaller the slope of the data in Figure 4.11, the better the position resolution. While the signal-to-noise ratio data in Figure 4.9 suggest that W13 would have the best position resolution, the data in Figure 4.11 suggest the opposite. This shows that signal-to-noise and P_{max} fraction data on their own are not sufficient to give an accurate depiction of position resolution, but rather, they must both be accounted for.

Fit Results for Position vs. Fraction Distribution

Wafer	$\frac{dx}{dF}$ (μm)
3	332.13
8	350.65
13	360.66
4	336.79

Table 4. Fit results for Position vs. P_{max} Fraction distributions. Increasing n^{+} concentration or dielectric thickness increases $\frac{dx}{dF}$.

After fitting the position vs. P_{max} fraction data in Figure 4.11 and finding values of $\frac{dx}{dF}$ for each wafer, these values, along with the signal-to-noise data in Figure 4.9, were plugged into Eq. 4 and the position resolution as a function of position was calculated for each wafer. The results are shown in Figure 4.12. The data show that σ_x ranges from about 8.6μm at the least precise down to 6.9μm at the most precise. The position resolution of each sensor improves near the pads. This is because fitting the position vs. P_{max} fraction data in Figure 4.11 to a line gave a constant value of $\frac{dx}{dF}$ for all positions, allowing the total signal-to-noise ratio distribution to determine the shape

of the position resolution distribution. Figure 4.12 shows that the position resolutions of wafers 8 and 13, which differ in n^+ concentration by a factor of two, are nearly indistinguishable, with differences of less than 1% on average. The maximum difference in position resolution between any two wafers is 5%. On average, however, the maximum difference in position resolution between wafers is approximately 3%. For a complete comparison of relative differences in position resolution between wafers, see Table 5. Given the low relative differences between wafers, a definitive dependence on n^+ concentration or dielectric thickness by the position resolution is not discernable. However, with position resolutions less than 10μm, each wafer displays improvements over what was previously possible with LGAD technology.

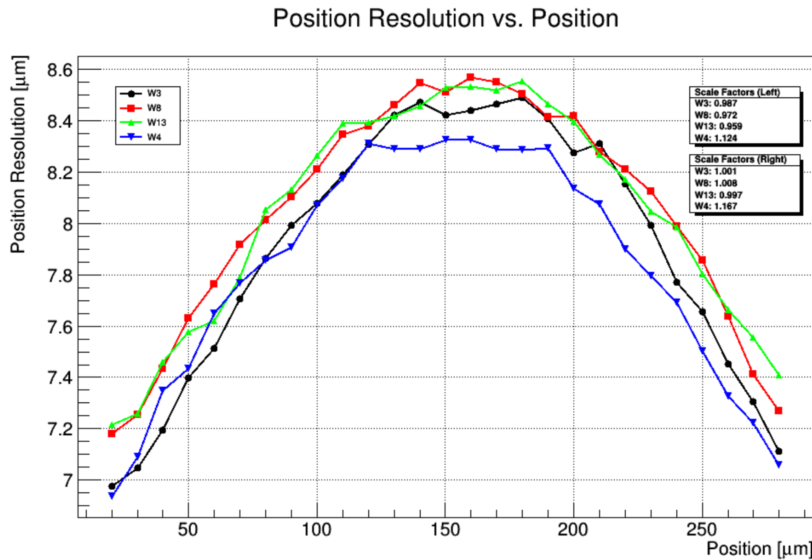

Figure 4.12. Position Resolution vs. Position for wafers 3, 4, 8, and 13. A position resolution between 7μm and 9μm is shown for each wafer. There is very little variation in position resolution between wafers (less than 5%) suggesting a weak dependence on n^+ concentration and dielectric thickness. The resolution of each sensor improves near the edges of the pads, where the signal-to-noise ratio is higher.

Relative Difference in Position Resolutions Between Wafers

Wafers Compared	Maximum Difference (%)	Average Difference (%)
W3 & W8	3	2
W3 & W13	4	2
W3 & W4	3	1
W8 & W13	2	1
W8 & W4	5	3
W4 & W13	5	3
Maximum difference between any two wafers (%)		5
Average maximum difference between wafers (%)		3

Table 5. Comparison of relative differences in position resolution between wafers.

4.3.1 Summary of Results for Position Resolution

This study examined how changing the n^+ concentration and dielectric thickness affected the spatial resolution of various AC-LGAD sensors. The spatial resolution in this experiment was affected by the total signal-to-noise ratio, $\frac{Sum(x)}{\sigma_n}$, and the inverse of the rate of change of F with respect to x, $\frac{dx}{dF}$. Each of these factors were found to have their own unique dependencies on n^+ concentration and dielectric thickness. Because of this, a straightforward trend relating the fabrication parameters of the AC-LGADs to the spatial resolution was not possible.

When examining the total signal-to-noise ratio vs. position distribution of each wafer, it was found that as n^+ concentration was increased, so was the total signal-to-noise ratio. For wafers 3 and 4 which have the same n^+ concentration but different dielectric thicknesses, it was found that a higher dielectric thickness, and thus lower capacitance, lead to a greater signal-to-noise ratio. From this information alone, because σ_x is inversely proportional to the total signal-to-noise ratio, it appeared that W13 would have the best spatial resolution. When examining the position vs. P_{max}

Fraction distribution, the fit results showed that $\frac{dx}{dF}$ decreased as n^+ concentration decreased. For wafers 3 and 4, the data showed that decreasing dielectric thickness also decreased $\frac{dx}{dF}$. Because σ_x is proportional to $\frac{dx}{dF}$, it would be expected that W3 would have the best spatial resolution, contrary to what the signal-to-noise data suggested.

The results were clarified only upon combining the information from the signal-to-noise data and position vs. P_{max} Fraction data. Using the signal-to-noise distributions and values of $\frac{dx}{dF}$ for each wafer, the spatial resolution, σ_x, of each wafer was calculated as a function of position between two adjacent pads. The data showed that the position resolution was least precise near the midway point between pads and most precise near the edges of the pads. This trend is due to the signal-to-noise distribution. Using a linear fit to calculate $\frac{dx}{dF}$ resulted in a single value of $\frac{dx}{dF}$ which in turn allowed signal-to-noise to determine how σ_x changed as a function of position for a given wafer. At the midway point between pads, σ_x ranged from about 8.3μm to 8.6μm whereas near the edge, σ_x ranged from about 6.9μm to 7.4μm. The maximum difference in position resolution across all wafers was found to be about 3% on average. As such, a definitive trend relating the AC-LGAD fabrication parameters to the position resolution could not be determined. Looking at the group of sensors as a whole, each wafer displayed position resolutions less than 10μm. Compared to sensors without charge sharing, with position resolutions given by the pad width divided by $\sqrt{12}$, which are limited to the millimeter scale (due to high requisite fill factor), the spatial

resolution of AC-LGADs show great potential for the next generation of particle detectors.

4.4 Timing Jitter

Achieving precise timing was the primary motivation for the development of LGADs. Timing information can be used in various different ways in particle physics. In the current use under development for the Large Hadron Collider, tracks reconstructed with conventional detectors will have their time tagged in an outer layer consisting of LGADs. This will allow the production time of the track to be measured, allowing it, in most cases, to be assigned to a unique production vertex.

In extremely dense tracking environments, it may become necessary to sort track-hit information from individual tracking layers according to their time of creation in the layer, in order to reduce the number of ways hits can be put together into tracks. For this, each tracking layer, and not just the outermost layer, would need to have the precision timing provided by LGADs. This approach is known as "four dimensional tracking".

A third possible use is to measure the time of flight of particles created in high energy collisions, in order to measure the speed of the given particle. If the particle momentum is measured independently, this will allow the mass of the particle to be measured, which will thus identify the type of particle.

In this study, the timing capabilities of AC-LGADs are examined in the form of the timing jitter, σ_j, given by Eq. 1. Although this is only one of several contributions to the timing resolution, it is the only one that is expected to vary from sensor to sensor. It also can be a dominant source for thin sensors, for which time smearing due to the statistics of the charge deposition process (the "Landau" contribution) can be small.

The timing jitter is the uncertainty placed on the time at which a given signal crosses a fixed threshold of the comparator which triggers a measurement. This uncertainty is due to an early or late firing of the comparator, resulting from the noise in the signal. This effect is shown in Figure 4.13. Because the signal noise is Gaussian and the jitter is directly proportional to the noise, by Eq. 1, the jitter of a given position is also Gaussian.

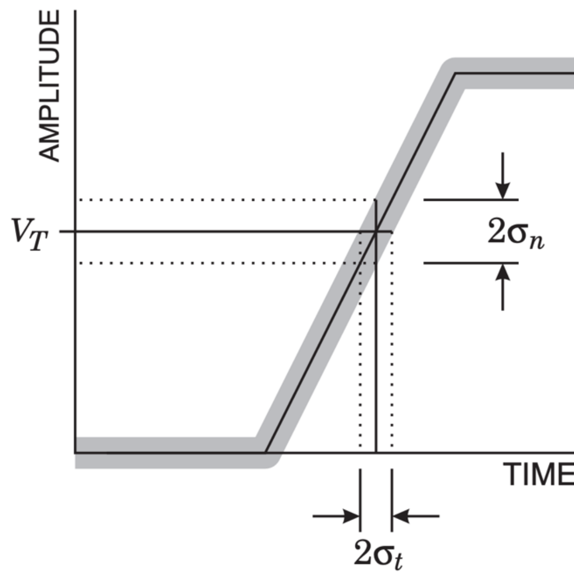

Figure 4.13. Effects of signal noise on comparator threshold crossing time. Signal noise causes early or late firing of the comparator, leading to uncertainties in the threshold crossing time proportional to the signal noise. Image taken from [11].

The timing jitter is made up of three components, as shown in Eq. 1, the rise time of the sensor, the signal of the sensor, and the noise of the readout as a whole. The amplifier used in these experiments was measured to have an RMS noise of about 2.5mV, uniformly for each channel. Accordingly, a fixed value of 2.5mV was used for the noise value in Eq. 1. The rise time of each sensor was roughly constant near the readout pad, but showed greater fluctuations past the halfway point between the pads.

Because of this, the measured rise time of each position was used in calculating the jitter, rather than using an approximate, fixed, value.

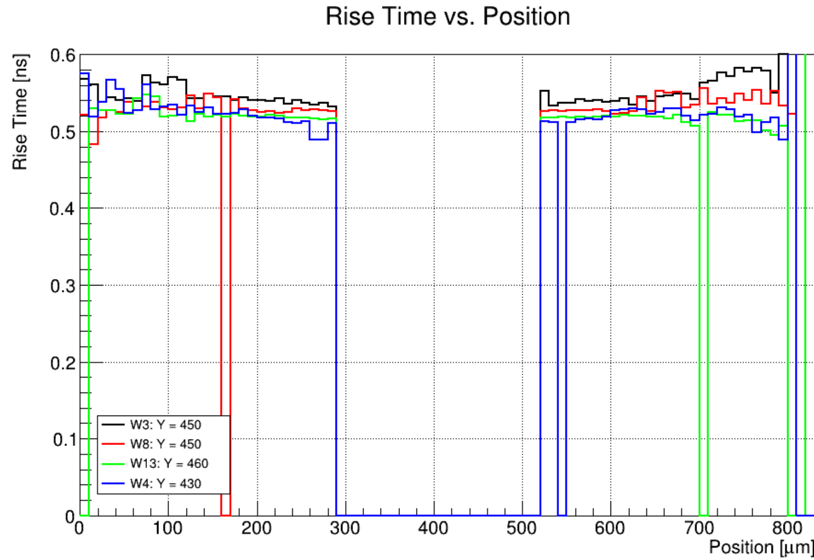

Figure 4.14. Rise time vs. Position for wafers 3, 4, 8, and 13. Slight differences in rise time are observed between wafers. For a given wafer, rise time is roughly constant within 100μm of the readout pad. After that, larger fluctuations begin to occur. Near the pad, W4 shows the smallest rise time, followed by W13, then W8, then W3. Past the midpoint between pads, the rise times of the four wafers begin to blend due to the increased fluctuations.

Figure 4.14 shows the measured rise time distribution as a function of position for each of the four sensors. The rise time distribution in Figure 4.14 is the distribution obtained by using the projection shown in figure 3.1. This projection is the same one used for the P_{max} distribution in Section 4.3. Slight differences in rise times between the different wafers were observed. For a given wafer, the rise time is roughly constant within 100μm of the readout pad. For signals past the midway point between pads, the rise times show larger fluctuations than those seen near the pads, making it difficult to order the sensors in terms of rise time. In the area of roughly constant rise time, near the pads, W4 was shown to have the shortest rise time, followed by W13, W8, then finally W3. The rise times in this region vary from about 0.51ns to 0.54 ns. Past the

midpoint, the rise times of the four sensors begin to blend due to the increased fluctuations.

The last component of the jitter is the sensor's signal. The P_{max} distributions used in this section were the same ones used in Section 4.3 for position resolution. From Figure 4.7 above, it is clear that the P_{max} distributions have a strong dependence on position. The signals of each sensor also vary between wafers. Like with the rise time, the P_{max} of each position was used to calculate the jitter of each sensor. The P_{max} and rise time distributions and the constant noise, 2.5mV, were plugged into Eq. 1 to calculate the timing jitter for each of the wafers studied.

Variations in jitter can be expected from both the differences in rise time as well as the differences in P_{max} between wafers. The differences in rise time and P_{max} are expected to come from two main sources. The first is a difference in n^+ concentration, which is discussed in Section 4.4.1. The second source is a difference in dielectric thickness, which is discussed in Section 4.4.2.

4.4.1 Timing Jitter n^+ Comparison

As mentioned above, the objective of this section is to characterize the effects of n^+ doping concentration on the timing capabilities of AC-LGADs. Referring back to Table 1, wafers 3, 8, and 13 have varying n^+ doping concentrations, with wafer 13 having the largest concentration (least resistivity) and wafer 3 having the smallest concentration (highest resistivity). Making use of their respective P_{max} and rise time distributions, as well as a fixed noise of 2.5mV, the jitter distributions of wafers 3, 8,

and 13 were plotted and overlaid with one another for comparison. This is shown in Figure 4.15 below.

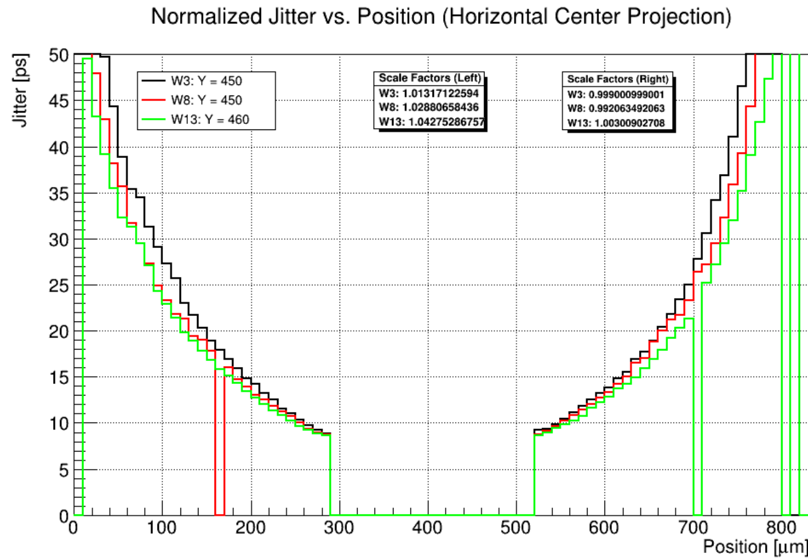

Figure 4.15. Normalized jitter profiles for wafers 3, 8, and 13, projecting horizontally through the center of the center pad. The cut out region from approximately 300-500μm represents the location of the pad. The profiles on either side of the pad were normalized independently to mimic the response to a MIP. Near the edge of the pad, a jitter of less than 10ps is observed, increasing to over 50ps approaching the adjacent pad edge. Jitter remains under 20ps out to about the midway point between pads. Wafer 13 has the lowest jitter, followed by W8, then W3. An overall trend is seen showing that as n^+ concentration is increased, jitter is decreased.

Shown in Figure 4.15 are plots of normalized jitter as a function of position for the horizontal projection through the center of the pad shown in Figure 3.1. Three data sets are shown, black, red, and green, representing wafers 3, 8, and 13, respectively. The cut away section from approximately 300-500μm in the plot represents the locations of the pads. Signal could not be measured in this location because the laser was not capable of penetrating the metal pad.

Near the edge of the pad, each wafer shows a jitter of less than 10ps. Additionally, they each maintain a jitter of less than 20ps out to about half way between

the pads. Near the edge of the neighboring pad, the jitters of each wafer climb to the vicinity of 50ps and above.

Regardless of position, the data in Figure 4.15 show that W3 has the highest jitter of the three, followed by W8, and W13 with the lowest. Recall from Table 1 that W3 has the lowest n^+ dose, corresponding to the highest sheet resistance, then W8, then W13, with the lowest sheet resistance. Accordingly, the data show overall that increasing the n^+ dose, or decreasing sheet resistance, results in a decrease in jitter.

As is seen in Figure 4.15, the jitter of a given pad rapidly increases as you move away from the pad. However, there are multiple pads on this sensor and it is observed that wherever the jitter of one pad increases to an impractically large amount, there is another pad with a low jitter. To further investigate this, the symmetry of the distribution was used to model the jitter distribution of a neighboring pad. As in Section 4.3 for position resolution, the jitter distribution to the right of the center pad was translated approximately 500µm to the left, creating a jitter distribution coming from the pad to the left of the one shown in Figure 4.15.

Using information from two pads, an effective jitter can be calculated with greater accuracy than what is obtained from using a single pad. As mentioned at the beginning of Section 4.4, the timing jitter is the uncertainty in the comparator threshold crossing time. By Eq. 1, the timing jitter is directly proportional to the signal noise and is therefore Gaussian. Accordingly, the threshold crossing time of a given position will have a variance of ${\sigma_j}^2$. Because the noise in separate channels is uncorrelated, the jitters

of two neighboring pads, measured in the same position, can be combined in the following way:

$$\sigma_{jw} = \sqrt{\frac{1}{\frac{1}{\sigma_{jL}^2} + \frac{1}{\sigma_{jC}^2}}} \tag{5}$$

where σ_{jL} and σ_{jC} are the jitters of left and center pads, respectively, at the same position on the sensor. Equation 5 is the uncertainty of the inverse-variance weighted average of the comparator threshold crossing time. In other words, it is the jitter of the time measurement made using information from two pads.

Using Eq. 5, the two neighboring jitter distributions were used to calculate the jitter of the weighted average of the threshold crossing time of the two pads, σ_{jw}. This is shown in Figure 4.16. Figure 4.16(a) shows the jitter distributions from Figure 4.15 alongside the weighted-average jitter distributions obtained from Eq. 5. Figure 4.16(b) shows the weighted-average jitter on its own. The benefits of using information from multiple pads are immediately made clear when looking at the differences between the weighted-average jitter and the jitter of a single pad in Figure 4.16(a). Where the jitter of a single pad continues to rise moving further away from the pad, the weighted-average jitter rises to a peak value at the midway point between pads then decreases moving towards the neighboring pad. Figure 4.16(b), on the other hand, provides a better understanding of how the different n^+ concentrations of wafers 3, 8, and 13 affect the overall timing jitter of the sensors.

Figure 4.16(b) shows that wafer 13 has the lowest weighted-average jitter, with a maximum value of about 12.3ps. Wafers 8 and 3 come after with maximum weighted-average jitters of about 13.4ps and 13.9ps, respectively. Near the edge of the pad, each wafer has a weighted-average jitter of about 8.5-9ps. The maximum difference in weighted-average jitter between wafers is approximately 13%. Taking into account the jitter measurements from two pads, the same trend is seen as with one pad; increasing n^{+} concentration results in a decrease in jitter.

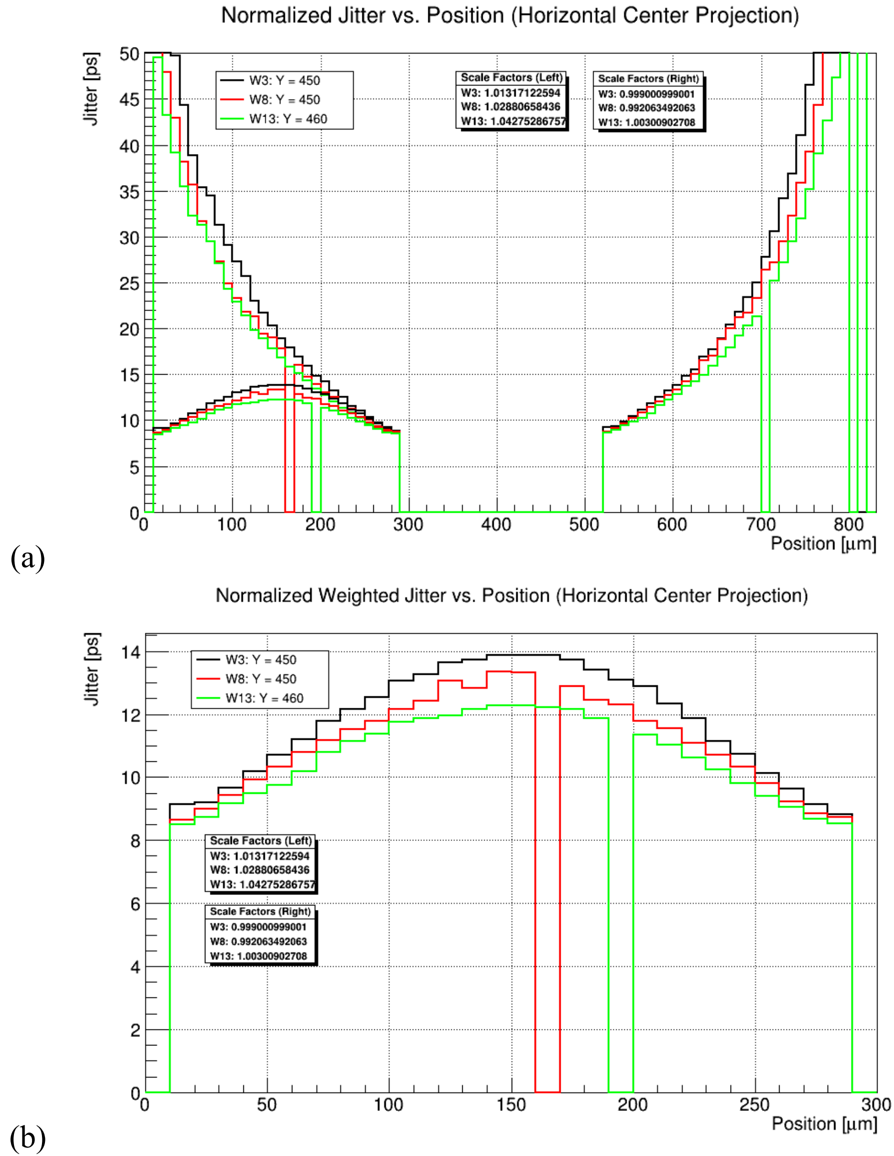

Figure 4.16. Weighted-average jitter profiles for wafers 3, 8, and 13 projecting horizontally through the center of the center pad. (a) shows the jitter profiles from Figure 4.15 alongside the weighted-average jitter obtained from modeling the jitter profile of a neighboring pad. (b) shows the weighted-average jitter on its own. At its least precise, in the midpoint between the pads, the weighted-average jitter is less than 15ps. Wafer 13 has the lowest jitter, followed by W8, then W3. The maximum difference in weighted-average jitter between wafers is approximately 13%. The weighted-average jitter distribution further affirms that as n^+ concentration is increased, jitter decreases. The spikes to zero seen in W8 and W13 are due to a failure to fit, not the sensor performance, and can be ignored.

4.4.2 Timing Jitter Dielectric Thickness Comparison

This section will examine how varying the thickness of the AC-coupling dielectric layer affects the timing capabilities of AC-LGADs. The wafers studied in this experiment were wafers 3 and 4. Referring back to Table 1, W3 has a “low” dielectric thickness and W4 has a “high” dielectric thickness. Accordingly, W3 will have the higher capacitance and W4 will have the lower. As in Section 4.4.1, each wafer’s respective P_{max} and rise time distributions, along with a fixed noise of 2.5mV, were plugged into Eq. 1 to calculate the jitter vs position distributions for each wafer. These distributions were plotted and overlaid with one another for comparison. This is shown in Figure 4.17.

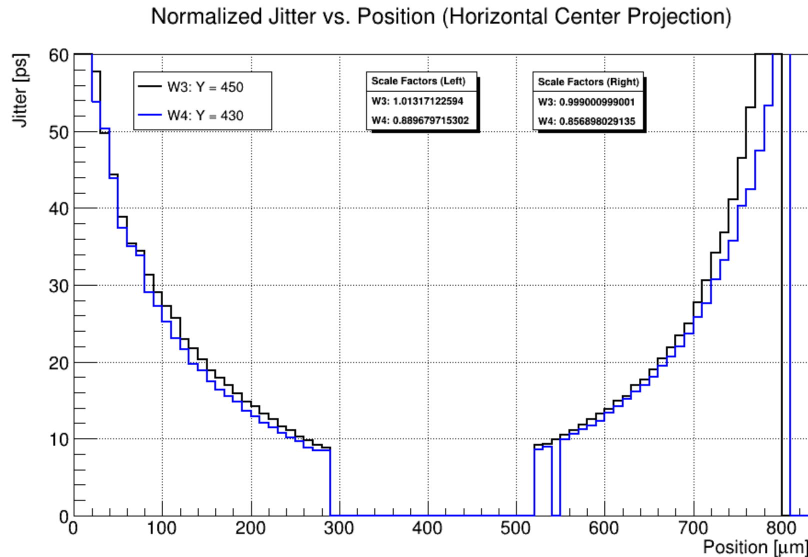

Figure 4.17. Normalized jitter profiles for wafers 3 and 4, projecting horizontally through the center of the center pad. The cut out region from approximately 300-500µm represents the location of the pad. The profiles on either side of the pad were normalized independently to mimic the response to a MIP. Near the edge of the center pad, a jitter of less than 10ps is observed, increasing to over 50ps near the adjacent pad edge. Jitter remains under 20ps out to about the midway point between pads. Wafer 4 has a lower jitter than W3, suggesting that as dielectric thickness is increased, jitter is decreased.

Shown in Figure 4.17 are plots of normalized jitter vs. position for wafers 3 (black) and 4 (blue). As in the previous section, they correspond to the horizontal projection going through the center of the pad shown in Figure 3.1 and the cut away section from approximately 300-500μm represents the locations of the pads where the laser could not penetrate the metal.

Figure 4.17 shows that W4 also shows a jitter of less than 10ps near the edge of the pad and a jitter less than 20ps out past the midway point between pads. The data show that W4 has a lower jitter than W3 regardless of position. This suggests that a higher dielectric thickness, or lower capacitance, results in a lower jitter.

For a better comparison between wafers, once again, the symmetry of the jitter distributions was used to model the jitter of a neighboring pad and calculate the weighted-average jitter of the two. The jitter distribution to the right of the center pad was translated approximately 500μm to the left to create a distribution coming from the pad to the left of the one shown in Figure 4.17 and the resulting distributions were plugged into Eq. 5. The weighted-average jitter distributions obtained are shown in Figure 4.18.

Figure 4.18(a) shows the jitter distributions from Figure 4.17 alongside the weighted-average jitter distributions obtained from Eq. 5. Figure 4.18(b) shows the weighted-average jitter on its own. The data further show that W4 has a lower jitter than W3. At its highest point, between the pads, W4 shows a jitter of about 13ps. Near the edge of the pad, W4 shows a jitter of about 8.5ps. The maximum difference in weighted-average jitter between wafers is approximately 10%. Ultimately, the data

suggest that as dielectric thickness is increased, or capacitance decreased, the jitter is decreased.

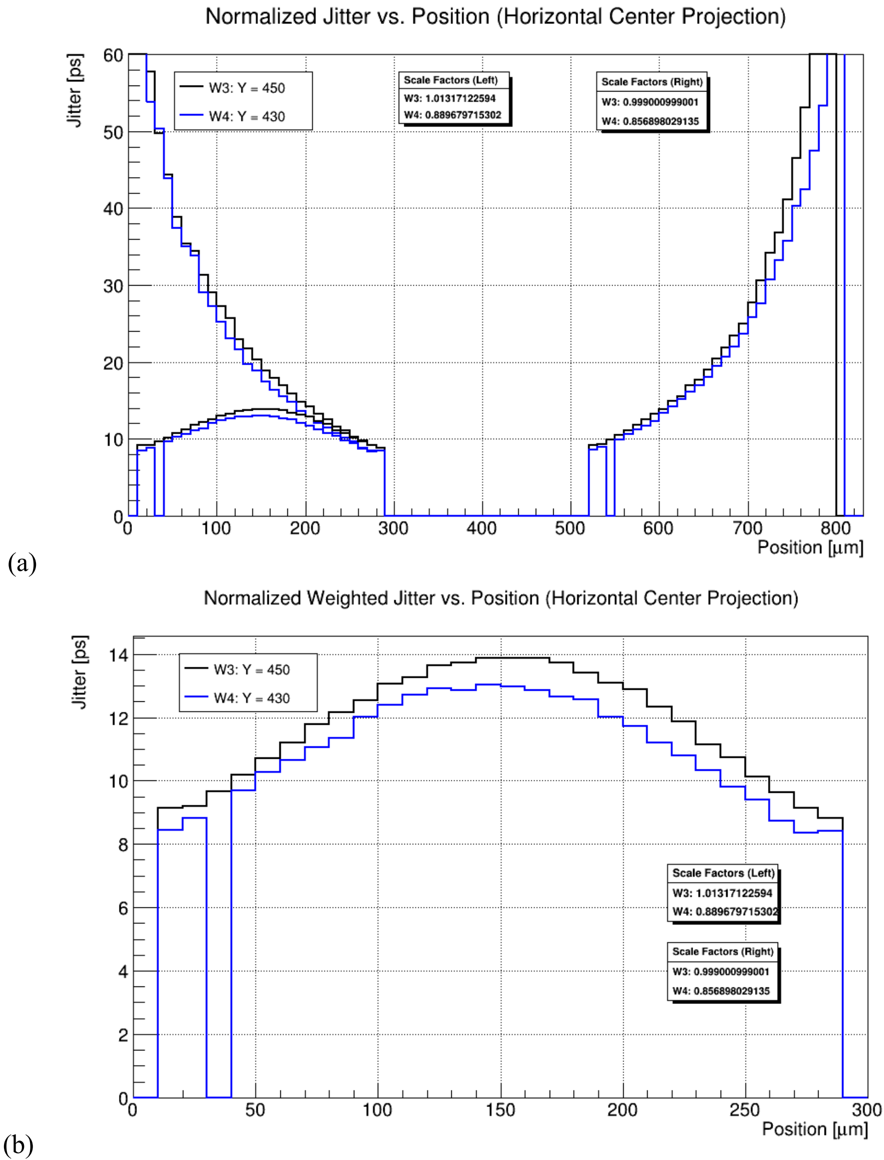

Figure 4.18. Weighted-average jitter profiles for wafers 3 and 4 projecting horizontally through the center of the center pad. (a) shows the jitter profiles from Figure 4.17 alongside the weighted-average jitter obtained from modeling the jitter profile of a neighboring pad. (b) shows the weighted-average jitter on its own. At its least precise, in the midpoint between the pads, the weighted-average jitter is less than 15ps. The maximum difference in weighted-average jitter between wafers is approximately 10%. Wafer 4 has a lower jitter than W3. The weighted-average jitter distribution further affirms that as dielectric thickness is increased, jitter decreases.

4.4.3 Summary of Results for Timing Jitter

In this study, the timing capabilities of various AC-LGAD sensors were characterized based on their n^+ doping concentrations and the thickness of their dielectric AC-coupling layers. The timing jitter, σ_j, of each wafer was calculated as a function of position between two adjacent pads. Using information from a single pad, both the n^+ comparison and the dielectric thickness comparison showed that a jitter of less than 20ps is possible to about the halfway point between pads. Near the edge of the neighboring pad, about 300μm from the pad being read out, σ_j increases to above 50ps.

By using information from multiple pads, in this case, two adjacent pads, σ_j can be greatly reduced. At the midway point between pads, where the weighted-average jitter, σ_{jw}, was at its maximum, σ_{jw} ranged from about 12.3ps to 13.9ps, depending on the wafer. Near the edge of the pads, where σ_{jw} was at its minimum, σ_{jw} ranged from about 8.5ps to 9ps. The maximum difference in weighted-average jitter between wafers ranged from 9-13% depending on the wafers compared. Overall, with σ_{jw} less than 15ps, each wafer demonstrates potential for high precision timing applications.

Changing the different fabrication parameters, n^+ concentration or dielectric thickness, several trends were observed. The n^+ comparison showed W13 had the lowest timing jitter, followed by W8, then W3. From Table 1, the order of n^+ concentration from highest to lowest is W13, W8, then W3. Therefore, the data suggest that as n^+ concentration is increased, timing jitter is decreased. Similarly, because the

level of n^+ concentration corresponds to the sheet resistance of the n^+ layer, the higher the n^+ concentration the lower the sheet resistance, it can also be said that a lower sheet resistance results in a lower timing jitter. The dielectric thickness comparison showed W4 had a lower jitter than W3. Wafer 4 has a higher dielectric thickness than W3, according to Table 1, and therefore has a lower capacitance than W3. The data then show that as dielectric thickness is increased, or capacitance decreased, jitter is decreased as well. In both studies, there was a definitive order relating the sensors' fabrication parameters to the timing jitter. The timing jitter is affected by both the rise time of the sensors and the signal-to-noise ratio. It was found that the contributions from rise time and signal-to-noise had the same effects on determining the rank order of timing jitter between wafers. Although the data show an order of highest to lowest timing jitter between wafers, the differences are, in general, very small (often on the order of 1ps or less). The greatest difference in σ_{jw} between any two wafers was about 2ps. While the timing jitter of the wafers overall is very good, further, application specific, investigation may be necessary to definitively distinguish the sensor with the best timing resolution.

5 Summary of Major Results

In this thesis, several different AC-LGAD fabrication configurations were studied in hopes of improving understanding for optimization of future sensor designs. Four different sensors were studied, wafers 3, 4, 8, and 13, all of which had the same pad geometry. Wafers 3, 8, and 13 differed only in their n^+ concentrations. Wafers 3 and 4 had identical n^+ concentrations but different dielectric thicknesses. The first study performed was a qualitative comparison of the average pulses of each of the different wafers. It was found that the results agreed with what would be expected by modeling the discharge of the pulse undershoots as an RC circuit. Comparing pulses between wafers with different n^+ concentrations showed that as dielectric thickness was increased, the magnitude of the undershoot was increased and the return to baseline time was decreased. Similarly, comparing pulses between wafers with different dielectric thicknesses showed that as dielectric thickness was increased, the magnitude of the undershoot was increased and the return to baseline time was decreased. Both of these experiments affirmed that reducing the sheet resistance (increasing n^+) or reducing capacitance (increasing dielectric thickness) would result in a smaller time constant (return to baseline time) of the equivalent RC circuit.

After examining how the pulse shapes of the different wafers behaved based on n^+ concentration and dielectric thickness, the pulse delay, t_d, of the different wafers was measured as a function of position. The resulting data were fit to a line to find the rate of change of delay with position. It was found that either increasing n^+ concentration or decreasing dielectric thickness both resulted in a decrease in the rate

of change of delay with position. The rates of change for the different wafers ranged from 0.28-0.47ps/µm. At distances from the readout pad greater than 100µm, each of these rates results in a delay that surpasses the current temporal resolution of standard DC-coupled LGADs. It is clear that to fully utilize AC-LGADs for precision timing measurements, a correction must be made that accounts for the increase in pulse delay with distance from the pad.

The third study examined how changing the n^+ concentration and dielectric thickness affected the position resolutions of the different wafers. Using information from two neighboring pads, the position resolutions of each of the four wafers were calculated. The data showed that position resolution was most precise near the edges of the readout pads, ranging from about 6.9µm to 7.4µm. The position resolution was least precise near the midway point between pads, ranging from about 8.3µm to 8.6µm. Across all wafers, the maximum difference in position resolution on average was less than 3%. There was no clear distinction as to which sensor had the best position resolution and thus, a trend relating the sensor fabrication parameters to the position resolution could not be determined.

The final study examined how changing the n^+ concentration and dielectric thickness affected the timing resolutions of the different wafers. The timing jitter of two neighboring readout pads was used to form a weighted-average jitter for the area between the two pads. Comparing weighted-average jitters between wafers differing only in n^+ concentration showed that as n^+ concentration increased, jitter decreased. Comparing weighted-average jitters between wafers differing only in dielectric

thickness showed that increasing dielectric thickness decreased the jitter. The weighted-average jitter was at its minimum near the edge of the readout pads where it ranged from 8.5ps to 9ps and was at its maximum at the midway point between pads where it ranged from 12.3ps to 13.9ps. The greatest difference in weighted-average jitter between any two wafers was about 13%. Of the four sensors, W13 was found to have the lowest jitter regardless of position.

Each of the sensors studied in this thesis demonstrated the precise timing and position tracking capabilities requisite of today's particle physics experiments. These results show the improvements upon LGAD technology made with the AC-LGAD system. With these improvements, the range of future particle physics research can be expanded allowing for novel understanding in the field.

Appendix A. Derivations of Silicon Sensor Signal Properties[1]

A.1 Maximum current signal in traditional silicon sensors

The Shockley-Ramo Theorem states that the current induced by a charge carrier is proportional to its electric charge, q, the charge's drift velocity, v, and the weighting field E_w:

$$i = qvE_w \tag{1}$$

In order to keep signal shape constant as a function of position, the drift velocity and weighting field must be kept constant. The easiest way to keep the drift velocity constant is to bias the sensor such that the resulting electric field causes the drift velocity to saturate.

$$v = v_{sat} \tag{2}$$

The weighting field is the component of the electric field in the direction of v that would exist at the location of the charge, q, under the following circumstances: the charge, q, is removed, the electrode on which the current is induced is at unit potential, and all other conductors are grounded [7], [9]. The best way to achieve a constant weighting field, given these circumstances is by constructing the sensor such that the readout pads and silicon closely resemble a parallel plate capacitor. In doing so, the weighting field, E_w, is inversely proportional to the thickness of the sensor.

$$E_w \propto \frac{1}{d} \tag{3}$$

Plugging (2) and (3) into (1) results in the following:

$$i \propto q\frac{1}{d}v_{sat} \tag{4}$$

Which gives the current induced in a silicon sensor by a charge carrier of charge q, when the sensor is biased such that the drift velocity is saturated, and with a weighting field resulting from a sensor geometry that resembles a parallel plate capacitor. Using (4), the maximum current in a pad sensor (parallel plate geometry), without gain, of thickness d, with a saturated drift velocity is given by:

$$I_{max} \propto Nq\frac{1}{d}v_{sat} = (n_{e-h}d)q\frac{1}{d}v_{sat} = n_{e-h}qv_{sat} \tag{5}$$

where $N = n_{e-h}d$ is the number of electron-hole pairs, given a charge creation of n_{e-h} electron-hole pairs per micron. (5) shows that for silicon sensors, the peak current is independent of sensor thickness.

[1] The derivations presented are a reproduction of those given in [1] and [8].

A.2 Dependence of signal slew rate on sensor gain and thickness

The value of the current generated by a gain, G, can be estimated in the following way: In a given time interval, dt, the number of electrons entering the gain layer is given by:

$$n_{e-h} v_{sat} dt \tag{6}$$

where n_{e-h} and v_{sat} are the same as in A.1. n_{e-h} is the electron-hole pair creation density due to the energy deposition of an incident particle and v_{sat} is the saturated drift velocity. These electrons generate

$$dN_{gain} \propto n_{e-h} v_{sat} dt \cdot G \tag{7}$$

new electron-hole pairs. Using the Shockley-Ramo Theorem once again, the current induced by these new charges is given by:

$$di_{gain} = dN_{gain} q \frac{1}{d} v_{sat} \tag{8}$$

Plugging (7) into (8) gives the following:

$$di_{gain} \propto (n_{e-h} v_{sat} dt \cdot G) q \frac{1}{d} v_{sat} \tag{9}$$

Dropping constants in (9), we arrive at the following relations:

$$di_{gain} \propto \frac{G}{d} dt \tag{10}$$

$$\frac{di_{gain}}{dt} \propto \frac{G}{d} \tag{11}$$

Because the amplifier used converts current to voltage, (11) can be rewritten as:

$$\frac{dV}{dt} \propto \frac{G}{d} \tag{12}$$

where V is the signal voltage. (12) shows that for sensors with a fixed gain, the slew rate is inversely proportional to sensor thickness.

A.3 Maximum current signal in silicon sensors with gain

As was done for a traditional silicon sensor, the maximum signal in a silicon sensor with gain can be calculated using the Shockley-Ramo Theorem.

$$I_{max} \propto N_{max} q \frac{1}{d} v_{sat} = (n_{e-h} d \cdot G) q \frac{1}{d} v_{sat} = n_{e-h} G q v_{sat} \tag{13}$$

Here, N_{max} is equal to the maximum number of charge carriers, $n_{e-h} d$ is the initial number of electron-hole pairs, and G is the gain. The remaining parameters are the same as those used in the previous derivations. (13) shows that the maximum signal current in a silicon sensor with gain depends only on the gain and not sensor thickness (assuming a saturated drift velocity).

References

[1] N. Cartiglia et al, “Design optimization of ultra-fast silicon detectors”, *Nucl. Instrum. Methods Phys. Res. A* 796 (2015) 141-148, http://dx.doi.org/10.1016/j.nima.2015.04.025

[2] N. Cartiglia et al, “Beam test results of a 16 ps timing system based on ultra-fast silicon detectors”, *Nucl. Instrum. Methods Phys. Res. A* 850 (2017) 83-88, http://dx.doi.org/10.1016/j.nima.2017.01.021

[3] CMS Collaboration, “Technical proposal for a MIP timing detector in the CMS experiment Phase 2 upgrade”, CERN-LHCC-2017-027, LHCC-P-009, http://cds.cern.ch/record/2296612

[4] “High-Luminosity Large Hadron Collider (HL-LHC): Preliminary Design Report”, CERN-2015-005, http://dx.doi.org/10.5170/CERN-2015-005

[5] M. Mandurrino et al, “Demonstration of 200-, 100-, and 50- µm Pitch Resistive AC-Coupled Silicon Detectors (RSD) With 100% Fill-Factor for 4D Particle Tracking”, *IEEE Electron Device Lett.* vol. 40 (2019) no.11, 1780-1783, https://doi.org/10.1109/LED.2019.2943242

[6] G. Pellegrini, “Technology developments and first measurements of Low Gain Avalanche Detectors (LGAD) for high energy physics applications”, *Nucl. Instrum. Methods. Phys. Res. A* 765 (2014) 12-16, http://dx.doi.org/10.1016/j.nima.2014.06.008

[7] S. Ramo, “Currents induced by electron motion”, *Proc. IRE* 27 (9) (1939) 584-585, http://dx.doi.org/10.1109/JRPROC.1939.228757

[8] H. F.-W. Sadrozinski, A. Seiden, N. Cartiglia, “4D Tracking with ultra-fast silicon detectors”, *Rep. Prog. Phys.,* vol. 81 (2018) 026101, https://doi.org/10.1088/1361-6633/aa94d3

[9] W. Shockley, “Currents to conductors induced by a moving point charge”, *J. Appl. Phys.* 9 (10) (1938) 635-636, http://dx.doi.org/10.1063/1.1710367

[10] H. Spieler, “FAST-TIMING METHODS FOR SEMICONDUCTOR DETECTORS”, *Lawrence Berkeley National Laboratory* (1982), https://escholarship.org/uc/item/2q95w8sh

[11] H. Spieler, “Semiconductor Detector Systems”, Oxford University Press (2005) [ISBN: 9780198527848]

[12] M. C. S. Williams, “Particle Identification using time of flight”. *J. Phys. Nucl. Part. Phys.* 39 (2012) 123001, http://dx.doi.org/10.1088/0954-3899/39/12/123001